

Rectifying Mask via Entropy for Distractor-Free 3DGS in Ambiguous Scenarios

Wongi Park¹ Jiyeon Lim² Minjae Lee³ Myeongseok Nam⁴ Seongjun Choi⁵
 Jungwoo Kim⁶ Soomok Lee^{†7} William J. Beksi^{†8} Sang-Hyun Lee^{†1}

¹Ajou University ²Samsung Electronics ³Georgia Institute of Technology ⁴GenGenAI
⁵Yonsei University ⁶Seoul National University ⁷Kennesaw State University ⁸University of Texas at Arlington

 [Code](#)  [Project page](#)  [Dataset](#)



Figure 1. Given real-world environments, RefineSplat effectively renders 3D novel view synthesis without ambiguous distractors. Our method effectively handles several challenging distractors (e.g., appearance variations, varying occlusions, dynamic objects, ambiguous distractors). To the best of our knowledge, this is the first work to pave the way for novel view synthesis in ambiguous real-world scenarios.

Abstract

We present *RefineSplat*, a systematic framework that effectively constructs transient masks to identify diverse ambiguous distractors. To do this, we qualitatively and quantitatively analyze issues and propose a novel entropy-aware adaptive masking method. Unlike existing approaches that struggle to distinguish transient elements from static scenes due to color or semantic ambiguity, *RefineSplat* captures ambiguous distractors leveraging entropy and instance masks. Furthermore, we propose a simple yet effective entropy-aware density control to align Gaussians in ambiguous scenarios considering Entropy-aware positional gradients. Additionally, to rigorously validate our method, we first create and release the *Ambiguous wild dataset*, including 18 scenes where distractors and static scenes are hard to distinguish due to color or semantic resemblances. Experimental results on various datasets demonstrate that *RefineSplat* shows state-of-the-art performance, showing

distractor-free novel view synthesis.

1. Introduction

Realistically rendering 3D scenes with 3D Gaussian Splatting (3DGS) [17] and Neural radiance field (NeRF) [34] from diverse real-world scenarios is a challenging and fundamental problem [11, 21, 32, 36, 59]. Unlike conventional methods [8, 14, 57] that primarily focus on constrained images which do not include distractors, this problem is characterized by the highly unstructured nature of the inputs (e.g., appearance variations, diverse distractors, dynamic objects, etc). To address these issues, existing methods [37, 40, 46] have tried to tackle unconstrained images, broadly falling into three paradigms. (1) Residual-based masking [25, 32, 39, 59] relies on photometric error to generate transient masks. (2) Semantic-based masking [11, 21, 63] exploits extracted features from DINOv2 [35] to identify distractors at the semantic level. (3) Heuristic-based masking [4, 31, 46] leverages extracted masks from

[†]Corresponding authors

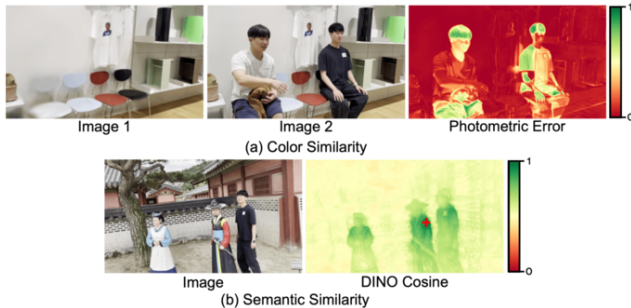


Figure 2. Motivation. We color the normalized values, ranging from **one to zero**. Ambiguous transient elements are difficult to distinguish due to color or semantic similarity.

SAM [19] using photometric error as a condition.

Challenges. Although prior methods [21, 28, 46, 49] show impressive results across real-world scenarios, these methods are still impeded by three limitations. (1) Leveraging photometric error makes it difficult to produce precise transient masks due to ambiguities, especially in cases where the background and distractors share similar colors. (2) Positional gradients based on photometric error for density control also degrade rendering quality by misaligning Gaussians in ambiguous scenarios. (3) Semantic-based masking [11, 21, 37], only leveraging extracted features from DINO [35], struggles with the challenge of semantic level similarity (e.g., moving vs stationary vehicles, a person vs a human-like statue).

Motivations and analysis. To understand how this issue emerges, we visualize our motivation in Fig. 2 and Fig. 7(a). Through this observation, we indicate that transient masks fail to capture distractors due to the color or semantic ambiguity between transient and static elements. Furthermore, we quantitatively and qualitatively confirm that the density control based on photometric error often misaligns Gaussians, as shown in Eq. 9 and Fig. 5. These limitations misalign Gaussians, degrading rendering quality.

Proposed solution. To address these limitations, we introduce RefineSplat, a novel framework that leverages entropy and boundary segments to capture ambiguous distractors. Specifically, we propose the entropy-aware adaptive masking, which utilizes entropy and instance masks. Furthermore, we propose the simple and yet novel entropy-aware density control strategy to mitigate misaligned Gaussians and align Gaussians, reducing artifact issues. To rigorously validate our method, we create and release the Ambiguous wild dataset, including 18 scenes where distractors and static scenes are difficult to identify due to color or semantic ambiguity. Through extensive experiments, we demonstrate that RefineSplat outperforms existing methods.

Key distinctions. To the best of our knowledge, RefineSplat is the first approach to capture ambiguous distractors leveraging entropy in real-world scenarios. This is not a trivial

extension of prior works, as it (1) formulates entropy-aware methods to capture ambiguous distractors; (2) utilize entropy magnitude to align Gaussians; and (3) constructs the Ambiguous wild dataset and consistently show impressive results in diverse real-world scenarios, whereas prior works are limited to two scenarios. Our major contributions can be summarized as follows:

- We introduce RefineSplat that leverages Entropy-aware adaptive masking, which integrates entropy and instance masks to capture ambiguous distractors.
- We propose the Entropy-aware density control that effectively aligns Gaussians, mitigating artifact issues.
- We create and release the Ambiguous wild dataset, comprising 18 challenging indoor and outdoor scenes where distinguishing distractors from static elements is particularly difficult due to color or semantic similarities.
- Extensive results demonstrate that RefineSplat achieves superior results over the state-of-the-art methods across diverse real-world scenarios.

2. Related Work

Novel view synthesis for unconstrained scenes. Most of the primary novel view synthesis methods [12, 17, 26, 34, 44] rely on the assumption of transient-free environments with consistent scenes. However, diverse real-world scenarios often violate these assumptions due to distractors. Numerous existing methods [25, 32, 34, 55] try to tackle these issues by constructing transient masks. NeRF-W [32] exploits an uncertainty embedding per view and a transient field which represent distractors to construct transient masks. CR-NeRF [55] propose a cross-ray paradigm and a grid sampling strategy for efficient appearance modeling. NeRF-MS [25] also utilizes transient embeddings and multi-sequence images captured with triplet loss. While NeRF-based methods [32, 34, 55] make effective transient masks, they still limit real-time rendering. 3DGS-based methods [17, 21, 53, 54], which is primarily advent, explicitly represent the 3D scene with differentiable rasterization, showing real-time rendering. Wild-GS [53] utilizes extracted depth maps from frozen Depth anything [54] to capture transient elements and preserve geometric consistency. WildGaussians [21] also utilizes extracted semantic features from frozen DINOv2 [35] to tackle transient elements. SpotlessSplats [40] leverage the power of diffusion model with clustering process to identify transient elements using photometric errors. Several methods [28, 36, 50] represent both static and transient elements by constructing transient fields. Specifically, ForestSplats [36] shows efficient memory usage to capture transient elements by adapting deformable MLPs. However, existing approaches [21, 25, 37, 46] primarily focus on either semantic features or residual maps, which makes it difficult to capture ambiguous distractors. In contrast, our method identifies am-

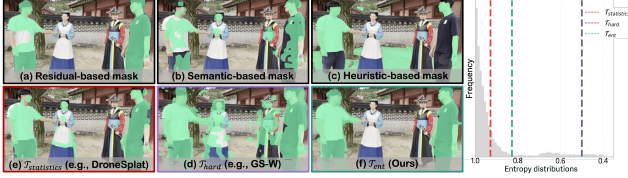


Figure 3. Effectiveness of transient masks and thresholds. (a) and (b) fail to capture distractors with similar color and semantics to static elements. (c) only focuses on extracted invariant masks from SAM before training. For the thresholds, (d) overestimates distractors. (e) is hard to capture ambiguous distractors, as it is heavily dependent on averages. However, (f) precisely captures ambiguous distractors in a skew distribution. (check color boundary)

ambiguous distractors by leveraging entropy and instance levels in real-world scenarios.

Adaptive density control. Unlike NeRF [34] with fixed parameter counts, 3DGS [17] represents 3D scenes using Gaussian primitives from 3D points. Recently, several works improve the densification strategy for various purposes: compressing [10, 22, 23, 62], structural encoding [6, 29, 61], and controlling density [2, 48, 56, 58]. However, most methods aim to work in constrained images, but their application to unconstrained images remains challenging due to transient elements. To tackle these challenges, several methods [16, 36] have emerged, offering robust densification strategies, reducing redundant Gaussians. RobustSplat [16] mitigates redundant Gaussians by leveraging delayed Gaussian growth. Unlike prior methods, we introduce an entropy-aware density control that aligns Gaussians, mitigating artifact issues in real-world scenarios.

3. Preliminary

3D Gaussian Splatting. 3D Gaussian Splatting (3DGS) represents a 3D scenes as an explicit set of anisotropic 3D Gaussians $\{\mathcal{G}_i\}$, each having a position $\mu_i \in \mathbb{R}^3$, covariance matrix $\Sigma_i \in \mathbb{R}^{3 \times 3}$, which is decomposed into scaling matrix $S \in \mathbb{R}^3$ and rotation matrix $R \in \text{SO}(3)$, opacity $\alpha_i \in [0, 1]$, and view-dependent colors $c_i \in \mathcal{C}^{N_{\text{SH}}}$ represented via spherical harmonics (SH) coefficients N_{SH} . To conduct 3D novel view synthesis, 3D Gaussians $\{\mathcal{G}_i\}$ are mapped to the image plane through the viewing transformation $W \in \mathbb{R}^{3 \times 3}$ and covariance matrix $\Sigma'_i = JW\Sigma_iW^TJ^T$ where $J \in \mathbb{R}^{2 \times 3}$ is the Jacobian of the Taylor approximation of the projective transformation. The pixel color $C(\mathbf{p})$ is computed by sorting the Gaussians according to depth and alpha blending:

$$C(\mathbf{p}) = \sum_{i=1}^N c_i \alpha_i \prod_{j=1}^{i-1} (1 - \alpha_j), \quad (1)$$

where $\alpha_i = \sigma(o_i) \exp(-\frac{1}{2}(p_i - \mu'_i)^\top \Sigma_i'^{-1}(p_i - \mu'_i))$. p_i and μ'_i are a pixel coordinate and a position of 2D Gaussian. All attributes of Gaussian $\{\mathcal{G}_i\}$ are optimized by minimizing

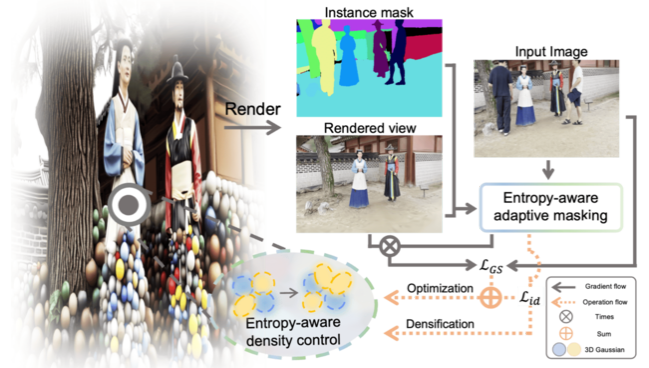


Figure 4. Overview of RefineSplat. We construct Entropy-aware adaptive masks by leveraging statistics of entropy and instance masks. Furthermore, we effectively align new Gaussians by utilizing entropy magnitude as a positional gradient and merging Gaussians across real-world scenarios.

the loss \mathcal{L}_{GS} between rendered image $\hat{I} \in \mathbb{R}^{3 \times H \times W}$ and ground truth image $I^{gt} \in \mathbb{R}^{3 \times H \times W}$ as follows:

$$\mathcal{L}_{\text{GS}} = (1 - \lambda)\mathcal{L}_1(\hat{I}, I^{gt}) + \lambda\mathcal{L}_{\text{D-SSIM}}(\hat{I}, I^{gt}), \quad (2)$$

where \mathcal{L}_1 is an L_1 loss, $\mathcal{L}_{\text{D-SSIM}}$ is a SSIM loss and λ is a weighting factor set to 0.2. All 3D Gaussians are initialized using a sparse point obtained from the Structure-from-Motion (SfM) approach such as COLMAP [42].

Adaptive density control. 3DGS and follow-up methods [2, 57] rely on the Adaptive Density Control (ADC) module to densify 3D Gaussians. ADC module periodically operates to densify 3D Gaussians considering positional gradient $\|\frac{\partial \mathcal{L}_{\text{GS}}}{\partial \mu}\|$ based on photometric error.

4. Method

Motivated by the preceding analysis, we introduce RefineSplat, which effectively captures ambiguous distractors that are difficult to distinguish due to color or semantic resemblance. As shown in Fig. 4, our method consists of two main components: (1) the entropy-aware adaptive masking, which leverages entropy and instance masks (Sec. 4.1). (2) Entropy-aware density control that leverage entropy magnitude to clone and splits Gaussians. Furthermore, we align Gaussians merging overlapping Gaussians (Sec. 4.2). Moreover, we introduce the consistency regularization to rectify incorrect instance masks (Sec. 4.3).

4.1. Entropy-aware adaptive masking

Entropy-aware local adaptive masking. To tackle ambiguous distractors, we leverage the 2D segmentation model [7] to obtain instance masks $\{\mathcal{M}_i^1, \mathcal{M}_i^2, \mathcal{M}_i^3, \dots, \mathcal{M}_i^K\} = S(I_i^{gt})$, where K is the number of instance masks, and \mathcal{M}_i^j denotes the mask of the j -th object in the image. Given these instance masks, we calculate the average entropy for each

instance as:

$$\bar{\mathcal{H}}_i^j = \frac{\sum_{p \in \mathcal{M}_i^j} (\mathcal{H}_i(p))}{|\mathcal{M}_i^j|}, \quad \mathcal{H}_i(p) = -\sigma(\mathcal{E}_i(p)) \log \sigma(\mathcal{E}_i(p)), \quad (3)$$

where \mathcal{E}_i is calculated as $\mathcal{E}_i = \psi_{id}(D_\theta(\hat{I}))$, $|\mathcal{M}_i^j|$ denotes the number of pixels in the instance mask, $\sigma(\cdot)$ denotes the sigmoid function, and $p \in \mathcal{M}_i^j$ indicates that p is one of the pixels contained within the mask \mathcal{M}_i^j . Specifically, we utilize a frozen MLPs ψ_{id} to extract entropy by leveraging extracted semantic features from DINOv2 D_θ , following prior works [21, 37, 63]. Although straightforwardly utilizing $\bar{\mathcal{H}}_i^j$ with fixed threshold is seemingly beneficial, leveraging $\bar{\mathcal{H}}_i^j$ with fixed threshold has limitations in clearly identifying distractors. To address these issues, several methods [37, 40, 46, 50] leverage thresholds based on statistical measures (e.g., mean, variance, percentile). However, these methods still struggle to handle the skewed distributions of $\bar{\mathcal{H}}_i^j$ that primarily arise in ambiguous scenarios where distractors have similar colors or semantic levels to static elements, as presented in Fig. 3. To overcome these problems, we introduce the adaptive entropy threshold \mathcal{T}_{ent} to identify ambiguous distractors with Shannon entropy [43] during training. For each iteration, we compute the optimal threshold \mathcal{T}_{ent} by maximizing the sum of entropy between the lower and upper subsets of the instance entropy distribution $\bar{\mathcal{H}}_i^j$ as follows:

$$\mathcal{T}_{ent} = \arg \max_t \left((1 - w_2) \mathcal{E}(\bar{\mathcal{H}}_i^j \geq t) + w_2 \mathcal{E}(\bar{\mathcal{H}}_i^j < t) \right), \quad (4)$$

where w_2 is a positive learnable weight factor used to adaptively adjust threshold. Finally, the local adaptive mask \mathcal{M}_{local} is constructed by selecting instances that exceed this optimized threshold as follows:

$$\mathcal{M}_{local} = \{ \mathcal{M}_i^j \mid \bar{\mathcal{H}}_i^j > \mathcal{T}_{ent}, j \in 1, \dots, K \}. \quad (5)$$

Entropy-aware global adaptive masking. Although relying solely on robust masks \mathcal{M}_{local} yields impressive results, this approach remains limited in handling fine-grained transient elements and incorrect extracted masks from SAM [19]. To address these, we leverage entropy and semantic features to globally identify subtle distractors as follows:

$$\mathcal{M}_{global} = \mathbb{1} \left\{ \left(\frac{\mathcal{U}_i}{\bar{\mathcal{H}}_i} \odot \mathbf{B}_{3 \times 3} \right) > \mathcal{T}_{glb} \right\}, \quad (6)$$

where $\mathcal{U}_i = \frac{2}{(\cos(D_\theta(I_i^{gt}), D_\theta(\hat{I}_i)) + 1)}$ is an uncertainty map, \mathcal{T}_{glb} is defined $\mathcal{T}_{glb} = \mathbb{E} \left[\frac{\mathcal{U}_i}{\bar{\mathcal{H}}_i} \right] + \text{Var} \left[\frac{\mathcal{U}_i}{\bar{\mathcal{H}}_i} \right]$, and $\mathbf{B}_{3 \times 3}$ is a box filter. $\mathbb{1}$ is an indicator function. Finally, the robust mask is defined as:

$$\mathcal{M}_{final} = \mathcal{M}_{global} \cup \mathcal{M}_{local}. \quad (7)$$

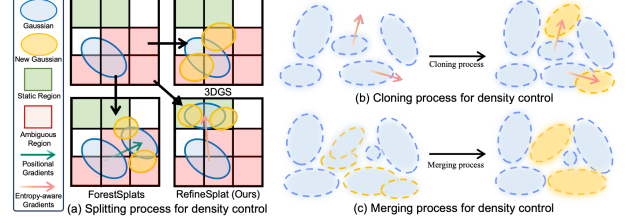


Figure 5. Entropy-aware density control. (a) Compared to existing methods, we split Gaussians utilizing entropy-aware gradients, aligning new Gaussians in static regions. (b) For the clone process, we generate new Gaussians following entropy-aware gradients. (c) We merge overlapping Gaussians considering color similarity, reducing redundant Gaussians and artifact issues.

By utilizing the robust mask \mathcal{M}_{final} , we more accurately capture ambiguous distractors independent of color and semantic similarity compared to prior methods. During optimization, the total loss is defined as:

$$\mathcal{L}_{GS} = (1 - \lambda) \mathcal{M}_{final} \odot \mathcal{L}_1(I_{pred}, I_{gt}) + \lambda \mathcal{M}_{final} \odot \mathcal{L}_{D-SSIM}(I_{pred}, I_{gt}). \quad (8)$$

4.2. Entropy-aware density control

Entropy-aware gradient for density control. Most prior methods [11, 36] utilize the derivation of \mathcal{L}_{GS} as a positional gradient in density control as:

$$\frac{\partial \mathcal{L}_{GS}}{\partial \mu} = \frac{\partial \mathcal{L}_{GS}}{\partial C} \frac{\partial C}{\partial \mu} = \frac{\partial \mathcal{L}_{GS}}{\partial C} \left(\frac{\partial C}{\partial c} \frac{\partial c}{\partial \mu} + \frac{\partial C}{\partial \alpha} \frac{\partial \alpha}{\partial \mu} \right). \quad (9)$$

Since the derivative of \mathcal{L}_{GS} primarily focuses on photometric error and density, aligning Gaussians during the density control remains challenging. This is particularly evident in regions where distractors share similar color or semantic features with the static background. Motivated by the limitations of photometric gradients, we propose the simple yet effective entropy-aware density control. This approach adaptively clones or splits Gaussians by incorporating entropy into the positional gradients, as shown in Fig. 5 and Eq. 10. To facilitate the cloning and splitting process in ambiguous regions, we derive the generation of new Gaussians based on the gradient of \mathcal{L}_{id} as follows:

$$\frac{\partial \mathcal{L}_{id}}{\partial \mu} = \frac{\partial \mathcal{H}}{\partial f_{pred}} \frac{\partial f_{pred}}{\partial D_\theta} \frac{\partial D_\theta}{\partial \hat{I}} \frac{\partial \hat{I}}{\partial \mu}, \quad (10)$$

where \mathcal{L}_{id} is defined as $\mathcal{L}_{id} = CE(\psi_{id}(D_\theta(\hat{I})), S(I_i^{gt}))$. Specifically, in contrast to ForestSplats [36], which relies on uncertainty embeddings and photometric error, our method effectively aligns Gaussians within the same identity by leveraging entropy. This approach mitigates artifact issues without requiring additional embeddings.

Merging process for overlapping Gaussians. After densification, we cluster and select pairs to merge Gaussians considering the overlap ratio and color similarity. This process

Method	Humanoid			Porter			Lounge			Bust			Jockey			Statuette		
	PSNR \uparrow	SSIM \uparrow	LPIPS \downarrow	PSNR \uparrow	SSIM \uparrow	LPIPS \downarrow	PSNR \uparrow	SSIM \uparrow	LPIPS \downarrow	PSNR \uparrow	SSIM \uparrow	LPIPS \downarrow	PSNR \uparrow	SSIM \uparrow	LPIPS \downarrow	PSNR \uparrow	SSIM \uparrow	LPIPS \downarrow
Mip-Splatting [57]	15.15	0.732	0.279	19.12	0.661	0.194	19.12	0.661	0.194	20.66	0.688	0.251	15.12	0.407	0.499	18.10	0.664	0.333
GS-W [59]	18.31	0.759	0.251	19.65	0.685	0.260	21.21	0.885	0.206	20.40	0.552	0.461	13.33	0.451	0.481	19.08	0.625	0.308
NexusSplats [47]	16.56	0.776	0.351	20.51	0.701	0.291	22.55	0.872	0.189	19.81	0.509	0.474	15.41	0.416	0.464	18.89	0.603	0.348
WildGaussians [21]	19.02	0.801	0.355	18.54	0.664	0.272	18.52	0.825	0.266	19.59	0.457	0.585	13.46	0.395	0.578	18.03	0.549	0.441
DroneSplat [46]	14.89	0.695	0.315	22.45	0.819	0.129	22.68	0.855	0.199	22.40	0.694	0.243	16.84	0.553	0.284	20.16	0.729	0.197
RobustSplat [11]	19.10	0.812	0.309	21.20	0.706	0.327	22.82	0.895	0.172	21.20	0.529	0.472	17.76	0.478	0.496	20.01	0.614	0.383
AsymGS [24]	19.53	0.828	0.272	22.38	0.810	0.131	21.53	0.889	0.198	21.26	0.696	0.245	17.02	0.489	0.331	20.12	0.714	0.237
RefineSplat(Ours)	19.71	0.841	0.173	24.30	0.873	0.128	23.14	0.902	0.143	22.91	0.708	0.225	18.45	0.588	0.308	22.04	0.758	0.194

Table 1. Quantitative results on the Ambiguous wild dataset. Performance is highlighted by color from third to first.

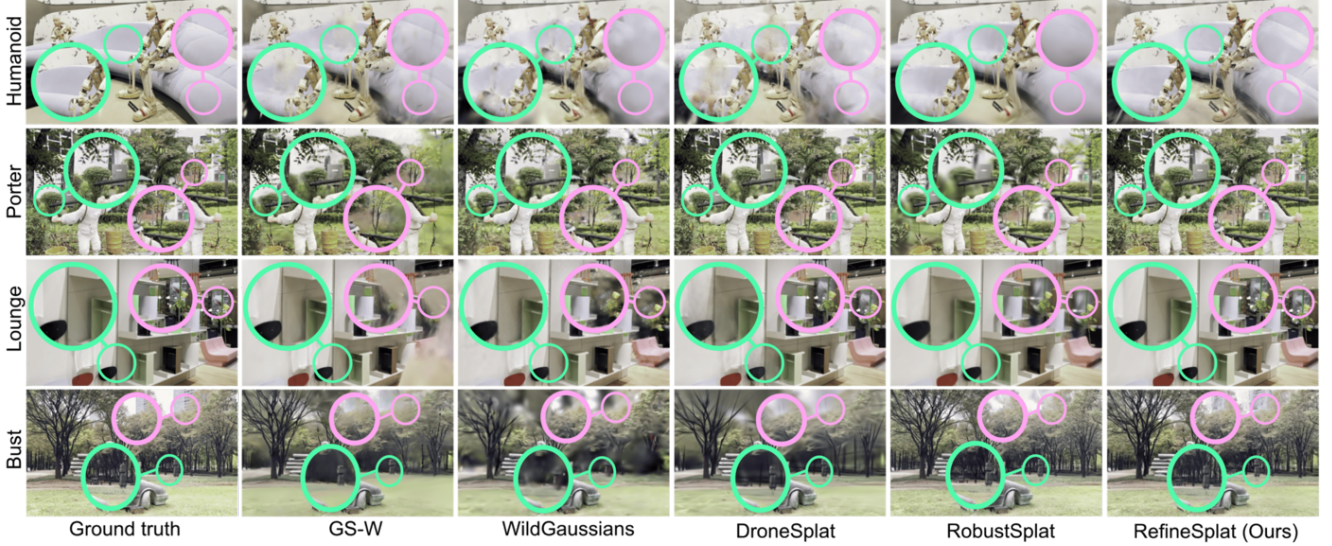


Figure 6. Qualitative results from novel-view synthesis on the Ambiguous wild dataset.

effectively reduces redundant Gaussians and mitigates artifacts from densification. The overlap ratio \mathcal{T}_{over} between the i -th and j -th neighboring Gaussians is defined as:

$$\mathcal{T}_{over} = \frac{\exp\left(-\frac{1}{2}(\mu_i - \mu_j)^\top (\Sigma_{sum})^{-1} (\mu_i - \mu_j)\right)}{\sqrt{(2\pi)^3 |\Sigma_{sum}|}}, \quad (11)$$

where Σ_{sum} is computed as $\Sigma_i + \Sigma_j$. For each clustered Gaussian, a new Gaussian with attributes $(\mu_k^*, c_k^*, \alpha_k^*, \Sigma_k^*)$ is defined by aggregating the Gaussians within each cluster in a weighted-based manner as:

$$\begin{aligned} \mu_k^* &= \frac{\sum_{i=1}^N \alpha_i \mu_i}{\sum_{i=1}^N \alpha_i}, & c_k^* &= \frac{\sum_{i=1}^N \alpha_i c_i}{\sum_{i=1}^N \alpha_i}, & \alpha_k^* &= \frac{\sum_{i=1}^N \alpha_i}{N}, \\ \Sigma_k^* &= \frac{\sum_{i=1}^N \alpha_i (\Sigma_i + (\mu_i - \mu_k^*)(\mu_k^* - \mu_i)^\top)}{\sum_{i=1}^N \alpha_i}, \end{aligned} \quad (12)$$

where N denotes the Gaussian number of clustered set. This merging process align and reduces redundant Gaussians.

4.3. Regularization and Optimization

Consistency regularization. Since the extracted instance masks [33] includes minor errors, we introduce the consistency regularization to rectify incorrect instance masks and

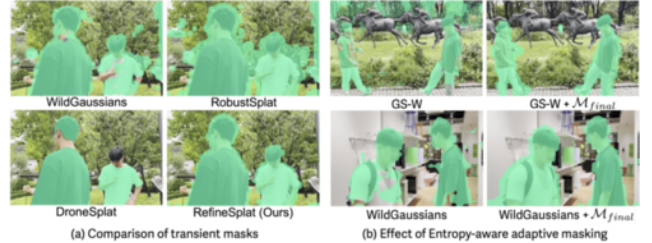


Figure 7. Analysis of the entropy-aware adaptive masking.

reduce the variance of entropy in segments, as follows:

$$\mathcal{L}_{cr} = \frac{1}{K} \sum_{j=1}^K \frac{1}{N^2} \sum_{p \in \mathcal{M}^j} \sum_{q \in \mathcal{M}^j} D_{KL}(\sigma(\mathcal{E}_i(p)) \| \sigma(\mathcal{E}_i(q))). \quad (13)$$

This encourages all pixels within each segment to represent a consistent identity, promoting precise transient masks.

Optimization. Finally, the total loss is defined as:

$$\mathcal{L}_{total} = \mathcal{L}_{GS} + \mathcal{L}_{id} + \alpha_1 \mathcal{L}_{cr}, \quad (14)$$

where α_1 is 0.2. During optimization, we periodically leverage the entropy-aware density control to align Gaussians. Furthermore, we also utilize the derivation of \mathcal{L}_{cr} to reflect entropy, cloning or splitting Gaussians, and effectively aligning Gaussians in real-world scenarios.

Method	NeRF On-the-go			Photo Tourism			Drone Imagery			Average		
	PSNR \uparrow	SSIM \uparrow	LPIPS \downarrow	PSNR \uparrow	SSIM \uparrow	LPIPS \downarrow	PSNR \uparrow	SSIM \uparrow	LPIPS \downarrow	PSNR \uparrow	SSIM \uparrow	LPIPS \downarrow
3D-GS [17]	19.30	0.668	0.252	18.03	0.814	0.183	17.12	0.622	0.301	18.15	0.701	0.245
HA-NeRF [5]	17.65	0.504	0.488	21.41	0.789	0.177	20.30	0.589	0.286	19.79	0.627	0.317
Mip-Splatting [57]	19.60	0.676	0.232	18.70	0.838	0.170	18.50	0.573	0.272	18.93	0.696	0.225
Splatfacto-W [52]	18.96	0.621	0.332	23.88	0.857	0.172	19.81	0.576	0.232	20.88	0.685	0.261
GS-W [59]	19.76	0.680	0.276	20.98	0.815	0.217	19.87	0.560	0.257	20.20	0.685	0.250
WildGaussians [21]	22.14	0.746	0.166	24.65	0.850	0.179	19.89	0.539	0.311	22.15	0.712	0.218
DroneSplat [46]	22.71	0.771	0.136	17.81	0.780	0.190	20.82	0.624	0.188	20.44	0.726	0.171
RobustSplat [11]	23.21	0.817	0.148	18.41	0.649	0.350	21.17	0.575	0.468	20.93	0.680	0.322
RefineSplat(Ours)	23.44	0.820	0.154	25.22	0.870	0.152	21.86	0.658	0.234	23.51	0.782	0.189

Table 2. Quantitative average results on diverse real-world datasets. Performance is highlighted by color, from third to first.

Method	w/ \mathcal{M}_{final}	Threshold			PSNR \uparrow	SSIM \uparrow	LPIPS \downarrow
		\mathcal{T}_{hard}	$\mathcal{T}_{statistics}$	\mathcal{T}_{ent}			
GS-W [59]	-	✓	-	-	20.31	0.868	0.251
	✓	-	-	-	21.17	0.874	0.243
	✓	-	✓	-	21.82	0.877	0.229
WildGaussians [21]	✓	-	-	✓	22.15	0.881	0.206
	-	✓	-	-	19.10	0.801	0.355
	✓	✓	-	-	19.84	0.847	0.302
	✓	-	✓	-	20.17	0.859	0.289
	✓	-	-	✓	20.31	0.861	0.283

Table 3. Ablation of the threshold with existing methods.

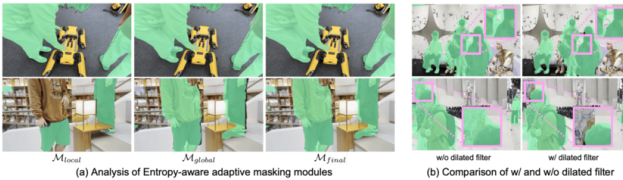


Figure 8. Analysis of the entropy-aware adaptive masking modules. (a) Analysis of Entropy-aware adaptive mask modules. (b) Comparison of w/ and w/o dilated filter.

5. Experiments

Implementation details. RefineSplat is developed based on DroneSplat [46] and RobustSplat [11]. All methods are trained following their own default settings. We train our method with 30K iterations, and the same learning rate as 3DGS [17] using RTX 4090 GPU on the Ambiguous wild and NeRF On-the-go [37] datasets. For the PhotoTourism [45] dataset, we train our method with 200k iterations. We also use the Adam optimizer [18] with weight decay. In addition, we utilize the frozen segmentation model [7] to utilize instance masks. Moreover, the semantic features used by the MLPs are extracted from frozen DINOv2 [35], using pre-trained weights from the distilled ViT-S/14 model. We also apply a down-sampling factor of 8 on the NeRF On-the-go and Ambiguous wild, following prior methods [11, 21]. We train 2-layer MLPs ψ_{id} using extracted instance masks, which takes just a few minutes before training the Gaussian field. Note that although our method can optimize the MLPs and the Gaussian field simultaneously, we first train the MLPs to simplify the overall pipeline.

Datasets, metrics, and baselines. We evaluate RefineSplat on three datasets: Photo Tourism [45], NeRF On-the-go [37], and Drone Imagery [46]. We propose the Ambigu-

	Entropy-aware adaptive mask		PSNR \uparrow	Humanoid SSIM \uparrow	LPIPS \downarrow
	\mathcal{M}_{local}	\mathcal{M}_{global}			
(a)	Baselines [11]	-	20.19	0.854	0.275
(b)	✓	-	21.33	0.873	0.198
(c)	-	✓	20.46	0.851	0.279
(d)	✓	✓	22.11	0.897	0.173

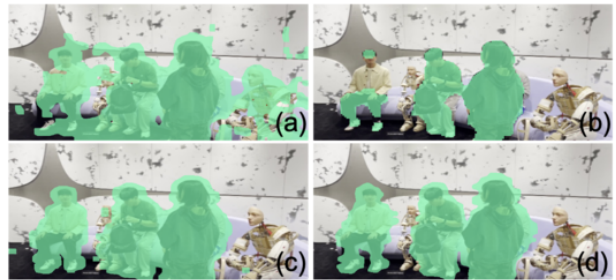


Table 4. Ablation of the entropy-aware adaptive masking.

	Entropy-aware density control		PSNR \uparrow	Jewel SSIM \uparrow	LPIPS \downarrow	Memory (MB)
	Entropy	Merging				
(a)	Baselines [11]	-	26.62	0.894	0.103	231.51
(b)	✓	-	27.43	0.911	0.095	186.09
(c)	-	✓	26.79	0.898	0.097	142.86
(d)	✓	✓	27.88	0.918	0.089	153.37

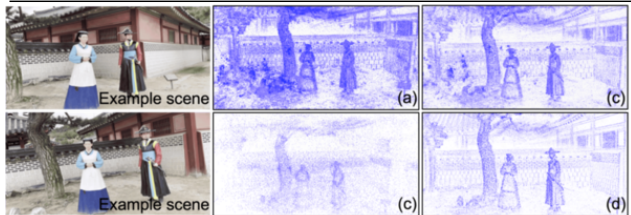


Table 5. Analysis of the entropy-aware density control.

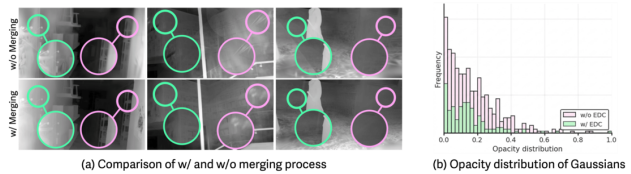


Figure 9. Analysis of the Entropy-aware density control. (a) Comparison of depth consistency w/ and w/o merging process. (b) Comparison of opacity distribution of Gaussians w/ and w/o entropy-aware density control (EDC).

ous wild dataset that contains 18 casually captured images, including 11 outdoor and 7 indoor scenes. To evaluate RefineSplat, we use PSNR, SSIM [51], and LPIPS [60] as met-

Scene	Method	Memory	Scene	Method	Memory
Humanoid	RobustSplat [11]	110.01	Patio	RobustSplat [11]	86.68
	DroneSplat [46]	51.32		DroneSplat [46]	114.13
	RefineSplat (Ours)	43.24		RefineSplat (Ours)	86.61
Spot	RobustSplat [11]	64.39	Sacre Coeur	RobustSplat [11]	82.15
	DroneSplat [46]	79.24		DroneSplat [46]	77.12
	RefineSplat (Ours)	25.80		RefineSplat (Ours)	31.26

Table 6. Analysis of memory usage in real-world scenarios.

	PUP	UAD	EDC (Ours)	PSNR \uparrow	SSIM \uparrow	LPIPS \downarrow	MB
(a)	✓			20.77	0.704	0.283	42.1
(b)		✓		21.16	0.719	0.271	39.5
(c)			✓	23.24	0.743	0.228	30.5



Table 7. Comparison of the density control strategy.

\mathcal{T}_{hard}	\mathcal{T}_{glob}	PSNR \uparrow	SSIM \uparrow	LPIPS \downarrow
✓	-	20.51	0.883	0.208
-	✓	21.18	0.891	0.197

Table 8. Impact of the entropy-aware adaptive global threshold on the Patio scene.

rics. We compare RefineSplat with prior work. (1) Residual-based masking: Ha-NeRF [5], 3DGS [17], Mip-Splatting [57], Splatfacto-W [52], GS-W [59]; (2) Semantic-based masking: WildGaussians [21], NexusSplats [47], RobustSplat [11]; (3) Heuristic-based masking: DroneSplat [46]. More baselines are included in the supplementary material.

Experimental analysis. For qualitative analysis, we show the rendering results of several methods [11, 21, 46, 59] as shown in Fig. 6. Furthermore, we also provide quantitative results as shown in Tab. 1 and Tab. 2. Compared to our method, RobustSplat [11] and WildGaussians [21], which only utilize extracted semantic features to capture distractors, struggle to tackle distractors that have similar semantic levels to static elements. GS-W [59] also only focuses on the residual map, which makes it hard to discern distractors that possess a similar color to the static background. DroneSplat [46] leverages heuristic invariant masks obtained from SAM [19] before training without error correction, which heavily depend on strict boundaries. In contrast to prior work, our method leverages entropy and instance masks to robustly capture ambiguous distractors.

6. Ablation Study

Effectiveness of the entropy-aware adaptive masking.

Although prior work primarily focus on photometric error or semantic similarity to identify transient elements, as presented in Fig. 7-(a), the entropy-aware adaptive masking distinguishes ambiguous distractors from static scenes by leveraging both semantic levels and instance levels. Furthermore, the entropy-aware adaptive masking can function as

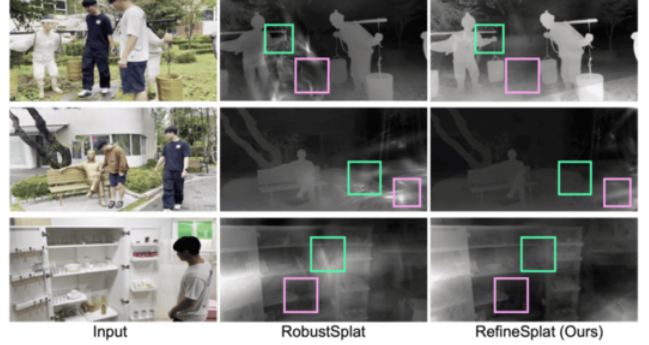


Figure 10. Comparison of the depth consistency. We visualize the depth consistency on the Ambiguous wild dataset.

a plug-and-play module, as shown in Fig. 7-(b) and Tab. 3. Although utilizing thresholds based on statistical measures (e.g., mean, variance, percentile) $\mathcal{T}_{statistis}$ or fixed values \mathcal{T}_{hard} show competitive results, it is struggle to capture diverse distractors in skew distributions, as depicted in Fig. 3. However, adding the entropy-aware adaptive masking to GS-W [59] and WildGaussians [21] effectively captures transient elements, showing robustness for \mathcal{L}_{ent} in ambiguous scenarios. We also illustrate how the entropy-based threshold works, as shown in Fig. 3. We also observe that leveraging global threshold \mathcal{T}_{glob} effectively constructs masks in capturing distractors compared to a fixed threshold \mathcal{T}_{hard} , as depicted in Tab. 8. Moreover, we observe that synthesizing the entropy-aware adaptive global and local masks plays a key role in creating robust transient masks by complementing their respective limitations, as shown in Tab. 4 and Fig. 8-(a). We observe that leveraging a box filter, following prior work [39, 40], considers neighboring context to capture distractors, as depicted in Fig. 8-(b). Through extensive analysis, we demonstrate that the entropy-aware adaptive masking precisely identifies ambiguous distractors.

Efficiency of the entropy-aware density control. As shown in Tab. 5, our strategy confirms memory efficiency compared to the baselines and arranges Gaussian anchors without artifacts. Furthermore, we observe that using the entropy-aware density control (EDC) reduces redundant Gaussians, leaving the number of high opacity Gaussians, as shown in Fig. 9-(a) and Fig. 9-(b). Moreover, to rigorously evaluate the effectiveness of the entropy-aware density control, we compare our methods with prior methods [11, 13, 36], as shown in Tab. 7, and Fig. 10. Although prior methods also show impressive results by utilizing photometric-based gradients, these methods struggle to align Gaussians in ambiguous scenarios. However, our method considers both entropy to align Gaussians, mitigating artifact issues. In addition, our method shows memory efficiency, maintaining visual quality, as shown in Tab. 6.

Analysis of the each module. As shown in Fig. 11, we confirm that the consistency regularization rectifies the er-

α_1	PSNR \uparrow	SSIM \uparrow	LPIPS \downarrow
0.1	21.74	0.882	0.186
0.2	22.11	0.897	0.173
0.3	21.62	0.879	0.191

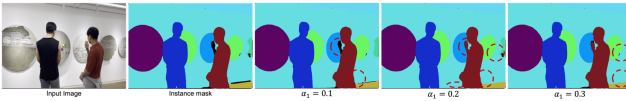


Table 9. Sensitivity analysis for α_1 values.

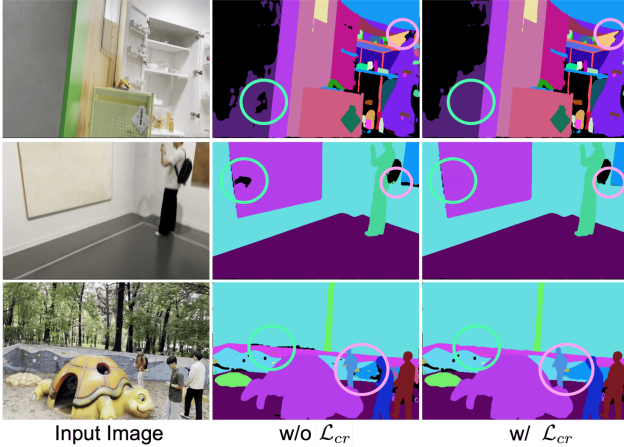


Figure 11. Analysis of the consistency regularization.

ror in instance masks. In addition, we examine the sensitivity to different hyperparameter settings, as shown in Tab. 9. The results indicate that the consistency regularization is robust to hyperparameter variations. Moreover, to analyze each module, we perform an ablation study to demonstrate the effectiveness: Entropy-aware adaptive masking (EAM), Entropy-aware density control (EDC), and Consistency regularization (CR), as shown in Tab. 10. The analysis shows that entropy-aware adaptive masking captures ambiguous elements. We also analyze how sensitive it is to patch sizes and DINO variants on the Patio scene, as shown in Tab. 11 and Tab. 12. Moreover, we continue to test dilation filter sizes, as shown in Tab. 13. We show more experiments for color threshold values for merging, as shown in Tab. 14. By observing them, we set a dilation filter size of 5.

Discussion on the Ambiguous wild dataset. We capture 18 natural scenes exemplifying different types of distractors, including varying ratios of distractors (from 5% to over 60%) and ambiguity, as shown in Fig. 12-(b). Furthermore, as illustrated in Fig. 2, to evaluate the ambiguity of the Ambiguous wild dataset, we consider three criteria: residual error, cosine similarity, and human evaluation (User Study). Moreover, we observe that leveraging COLMAP [41] on the Ambiguous wild dataset, where distractors and static elements are visually or semantically similar, tends to produce incorrect matching points, which hinders the initialization of Gaussians, as shown in Fig. 12-(a).

	EAM	EDC	CR	Ambiguous wild			NeRF On-the-go		
				PSNR \uparrow	SSIM \uparrow	LPIPS \downarrow	PSNR \uparrow	SSIM \uparrow	LPIPS \downarrow
	Baseline [11]			20.52	0.756	0.277	22.14	0.746	0.166
(a)	✓	-	-	22.73	0.834	0.163	22.78	0.808	0.159
(b)	✓	-	✓	23.46	0.858	0.154	23.13	0.811	0.157
(c)	✓	✓	-	23.14	0.842	0.158	23.29	0.812	0.156
(d)	✓	✓	✓	23.83	0.868	0.149	23.44	0.820	0.154

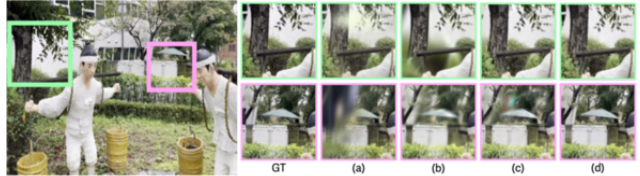


Table 10. Impact of each module. We show impact of each module on NeRF On-the-go and Ambiguous wild datasets.

Methods	PSNR \uparrow	SSIM \uparrow	LPIPS \downarrow
DINO 14 \times 14	23.44	0.820	0.154
DINO 16 \times 16	23.37	0.817	0.149

Table 11. Sensitivity of size.

Filter Size	PSNR \uparrow	SSIM \uparrow	LPIPS \downarrow
3 \times 3	21.74	0.882	0.186
5 \times 5	22.10	0.897	0.173
7 \times 7	21.32	0.853	0.192

Table 13. Sensitivity of filters.

Threshold	PSNR \uparrow	SSIM \uparrow	LPIPS \downarrow
DINOv1	23.64	0.865	0.131
DINOv2	24.30	0.902	0.128

Table 12. Sensitivity of DINO.

Threshold	PSNR \uparrow	SSIM \uparrow	LPIPS \downarrow
0.10	23.64	0.895	0.154
0.15	23.87	0.902	0.143
0.20	23.45	0.891	0.157

Table 14. Threshold of EDC.



Figure 12. Analysis of the Ambiguous wild dataset. (a) Initialization of Gaussians. (b) Examples of the Ambiguous wild dataset.

7. Limitation and Conclusion

Limitations. RefineSplat captures ambiguous elements leveraging entropy and instance masks. However, there are still two limitations in some cases. Firstly, since RefineSplat leverages vision foundation models, the performance can fluctuate depending on foundation models. Secondly, utilizing sparse views still struggles to generalize visual results. Future work may integrate diffusion models to inpaint sparse or corrupted regions in the Gaussian field.

Conclusion. We present RefineSplat, a novel framework for handling ambiguous distractors in diverse real-world scenarios. RefineSplat captures ambiguous distractors with Entropy-aware adaptive masking and aligns Gaussians through Entropy-aware density control. We also release the Ambiguous wild dataset with 18 scenes where distractors and static scenes are difficult to distinguish due to color or semantic ambiguity. Extensive results demonstrate the robustness and capability of our method.

In this supplementary material, we provide additional discussion and experimental results due to page limitations. Moreover, we also discuss future directions. The contents are summarized as follows:

- Sec. A: Key distinctions.
- Sec. B: Descriptions of the Ambiguous wild dataset.
- Sec. C: Implementation details.
- Sec. D: Experiment results.
- Sec. E: Ablation studies.
- Sec. F: Future works.

A. Key distinctions

Key distinction from DroneSplat. Although RefineSplat leverages Grounded SAM [7], there are significant technical differences from DroneSplat [46]. (1) DroneSplat constructs transient masks using instance masks with photometric error, which makes it hard to capture ambiguous distractors with similar color and semantics to static elements. However, our method effectively captures ambiguous distractors considering entropy. (2) DroneSplat densifies Gaussians considering photometric error, which misaligns and causes artifact issues in the Gaussian field. In contrast, RefineSplat shifts Gaussians considering entropy, which aligns them at the instance level. (3) DroneSplat utilizes statistical measures to construct a threshold in capturing distractors. However, it is hard to identify distractors in a skewed distribution. Compared to DroneSplat and several methods [21, 37, 55] that utilize a fixed threshold, RefineSplat captures ambiguous distractors and consistently shows robustness in diverse real-world scenarios, as shown in Fig. 13.

Key distinction from SpotlessSplats. SpotLessSplats [40] utilizes semantic features to capture distractors. Despite RefineSplat also leveraging semantic features, it significantly differs from SpotLessSplats in constructing masks. (1) SpotLessSplats highly depends on extracted semantic features from the diffusion model to construct transient masks using photometric error as a condition in training MLPs. However, RefineSplat constructs robust masks by considering instance masks and entropy. (2) SpotLessSplats uses fixed thresholds to define bounds for photometric error, constructing masks with a fixed percentile value. However, RefineSplat adaptively adjusts a threshold considering a skew distribution, showing impressive results in diverse scenarios.

Key distinction from compression methods. Several works [2, 15, 22, 30] focus on memory compression through hashing and pruning in constrained scenes. RefineSplat densifies and merges Gaussians to effectively align Gaussians, enhancing rendering qualities in real-world scenarios that include diverse distractors. In the process, RefineSplat also achieves memory efficiency as a side effect, showing high-quality rendering results.



Figure 13. Analysis of threshold strategies. We visualize how threshold strategies affect the robustness of the transient mask in ambiguous scenarios.

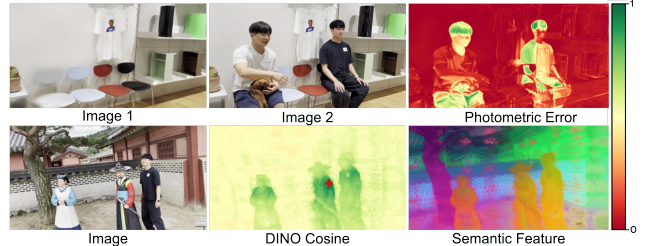


Figure 14. Visualization of residual and cosine similarity maps. We color the normalized values, ranging from **one to zero** in ambiguity scenes. The first row is hard to identify static and transients due to color similarity. The last row is challenging to capture transient images due to feature similarity.

B. Descriptions of the Ambiguous wild dataset

Details of dataset acquisition. The Ambiguous wild dataset consists of 18 scenes captured with an iPhone 12 Pro and a Samsung Galaxy S22. The acquisition process follows previous methodologies [37, 39] to ensure consistency. During each capture, exposure, white balance, and ISO were kept fixed. This dataset contains diverse visually ambiguous scenarios where transient and static elements exhibit similar colors or semantic levels (e.g., moving vs parked vehicles, a real person vs a mannequin). Furthermore, scenes include varying occlusion ratios ranging from 5% to 45%. The images were captured using an iPhone 12 Pro and a Samsung Galaxy S22, with all images recorded at a resolution of 1920×1080. We show samples of each scene in Fig. 18 and Fig. 19.

Evaluation of ambiguity. To evaluate the ambiguity of the Ambiguous wild dataset, we consider three criteria: residual error, cosine similarity, and human evaluation (User Study). For color similarity, we define color ambiguity as occurring when more than 30% of the pixels have a color difference of less than 0.3 between distractors and the background, distinguishing transient elements from the static background. For semantic similarity, a scene is considered ambiguous if the cosine similarity between distractors and static objects (e.g., sculptures or mannequins) exceeds 70%, as presented in Fig. 14. Furthermore, to rigorously evaluate ambiguity in our Ambiguous wild dataset, we conduct a user study, as shown in Fig. 30. The results from the human evaluation, conducted via a Google Form survey and Amazon Mechanical Turk, clearly demonstrate the presence of ambiguity in our Ambiguous wild dataset, including objects that exhibit similar semantic levels or colors compared to static scenes.

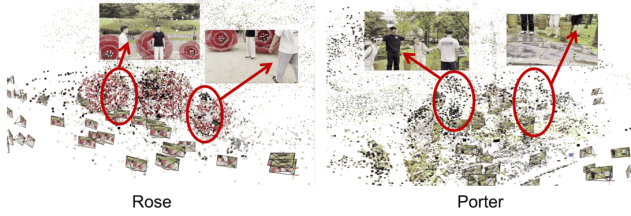


Figure 15. Effectiveness of COLMAP SfM point clouds due to ambiguous distractors.

Moreover, we observe that leveraging COLMAP [41] on the Ambiguous wild dataset, where distractors and static elements are visually or semantically similar, tends to produce incorrect initialization of Gaussians, as shown in Fig. 15.

Author statement of data license. The authors of the Ambiguous wild dataset affirm that the dataset was collected, processed, and released in full compliance with applicable ethical guidelines and regulations. We assume full responsibility for any potential violations of rights or ethical standards arising from its use. The Ambiguous wild dataset is made freely available under the CC BY-NC-ND 4.0 license, allowing unrestricted sharing and downloading in any medium and repositories, as long as the authors are properly credited, it is used for non-commercial or research purposes, and no derivative works are made.

C. Implementation details

Implementation details. For training RefineSplat, we conduct the densification interval of 3D Gaussians with hyperparameter settings following RobustSplat [11]. For weighting factors w_2 , we adopt the sigmoid function to ensure positive constants. To leverage semantic features, we resize the images to extract semantic features from DINOv2 [35]. We also use NerfBaselines [20] for fair comparison. Furthermore, we describe notation to understand our method more easily, as presented in Tab. 24. For the frozen MLPs ψ_{id} , we pre-train MLPs ψ_{id} using extracted 2D instance masks from Grounded SAM [7] and semantic features with Adam optimizer [18], following the main Eq. 10. Moreover, we add a small perturbation to the denominator of main Eq. 6 to prevent the zero-division problem. Moreover, to make understanding easier for readers, we provide procedures of merging in Algorithm 1.

Additional baselines. We include more baselines (*e.g.*, T-3DGS [31], SpotLessSplats [40], DeSplat [49], HybridGS [28], ForestSplats [36], SWAG [9]) to further validate the effectiveness of our method. Note that for methods without publicly available code, we omit memory usage, and the performance results are reported from the original papers.

Details of adaptive entropy threshold. To address skewed distributions in ambiguous scenarios, we calculate the adap-

Algorithm 1: Merging Pipeline

Input: Rendered image \hat{I} , GT image I^{gt} , transient masks \mathcal{M}_{final} , and instance masks \mathcal{M}_{ins}

- 1 **Initialization:**
 $\mu, S, R, \alpha, c \leftarrow$ Structure-from-Motion (SfM)[41]
- 2 **for** i **in** $(1, \dots, N)$ **do**
 - /* Render and Optimize the 3D representation */
 - 3 $\mathcal{L}_{total} \leftarrow \mathcal{L}_{GS}(\hat{I}, \tilde{I}^{gt}, \mathcal{M}_{final}) + \mathcal{L}_{id}(\hat{I}, \tilde{I}^{gt}, \mathcal{M}_{ins}) + \mathcal{L}_{cr}(\hat{I}, \mathcal{M}_{ins})$
 - 4 $\mu, S, R, \alpha, c \leftarrow Adam(\nabla \mathcal{L}_{total})$
 - 5 **if** $IsEntropyDensityControl(i)$ **then**
 - 6 Densification(\mathcal{G})
 - 7 **if** $IsMerging(i)$ **then**
 - 8 **for** Gaussians $\mathcal{G}_i(\mu, S, R, \alpha, c)$ **do**
 - 9 **if** $\nabla \mathcal{L}_{total} < \tau_e$ **then**
 - 10 **for** k -neighbor Gaussians $\mathcal{G}_j(\mu, S, R, \alpha, c)$ **do**
 - 11 $\mathcal{O} \leftarrow$ Overlap Ratio($\mathcal{G}_i, \mathcal{G}_j$) Eq. 11
 - 12 **if** $ColorResidual(c_i, c_j) < 0.15$ **and** $\mathcal{O} > 0.3$ **then**
 - 13 | Merging($\mathcal{G}_i, \mathcal{G}_j$)
 - 14 | **end**
 - 15 | **end**
 - 16 | **end**
 - 17 | **end**
 - 18 | **end**
 - 19 **end**
 - 20 **end**

tive entropy threshold using Shannon entropy [43] as:

$$\mathcal{E}(\mathcal{H}) = - \sum_{i=1}^N \mathcal{H}_i \log(\mathcal{H}_i). \quad (15)$$

By utilizing them, we show robustness in constructing transient masks in a skew distribution compared to existing methods, as shown in Fig. 13.

D. Experiment results

Comparison on the Ambiguous wild Dataset. We present qualitative results and quantitative results, as presented in Fig. 20, Fig. 21, Tab. 15, and Tab. 16. Although DroneSplat [46] shows reasonable performance, DroneSplat [46] has difficulty handling ambiguous scenes where transient and static elements exhibit similar colors or share semantically similar features, due to only considering residual maps to utilize extracted masks from SAM [19]. Furthermore,

DroneSplat [46] depends exclusively on extracted transient masks from SAM [19] before training, making it less capable of handling ambiguous distractors in diverse real-world scenarios. Despite RobustSplat [11] and NexusSplats [47] showing competitive performances, RobustSplat [11] and NexusSplats [47] primarily focus on semantic features, which makes it difficult to identify ambiguous distractors that have semantic levels similar to static elements. In contrast, RefineSplat not only effectively removes ambiguous distractors but also shows impressive results leveraging entropy and instance masks. Furthermore, RefineSplat shows effective transient masks in handling ambiguous distractors, as depicted in Fig. 25 and Fig. 26. Furthermore, RefineSplat shows memory efficiency compared to baselines, as shown in Tab. 20 and Tab. 21.

Comparison on the NeRF On-the-go Dataset. As presented in Fig. 22 and Tab. 17, RefineSplat achieves high-quality rendering results and shows competitive performance. Compared to SpotLessSplats [40], which primarily relies on the diffusion process [38], our method exhibits faster training speed while eliminating diverse distractors. Although HybridGS [28], DeSplat [49], and GS-W [59] also show great results, they have difficulty capturing transient elements that possess color similarity. Furthermore, RobustSplat [11] and WildGaussians [21] also show impressive results by leveraging semantic features. While semantic features are useful for handling uncertainty in distractors, distinguishing them from static scenes that have a similar semantic level to distractors remains challenging. However, our method leverages instance masks to identify ambiguous distractors, which is effective in capturing diverse distractors, as illustrated in Fig. 27. Moreover, we show details of memory usage in Tab. 22. It implies that leveraging the entropy-aware density control improves memory efficiency compared to baselines. Note that we report the total runtime for SpotLessSplats [40], which is the sum of the Diffusion feature extraction time and the training time.

Comparison on the Photo Tourism Dataset. We provide additional qualitative and quantitative results, as shown in Fig. 23 and Tab. 18. Although WildGaussians [21] and NexusSplats [47] provide quantitatively remarkable results, those methods only focus on interpolated semantic features, which makes it difficult to capture fine-grained details of distractors. While RobustSplat [11] and DroneSplat [46] also show impressive results on the NeRF On-the-go [37] and Ambiguous wild datasets, they are hard to tackle appearance variation on the Photo Tourism [45] dataset due to a lack of appearance modeling. GS-W [59], SWAG [9], and DeSplat [49] also show impressive results by considering only the residual map to identify transient elements. However, it is difficult to detect distractors that have similar colors to static scenes. To understand these challenges, we

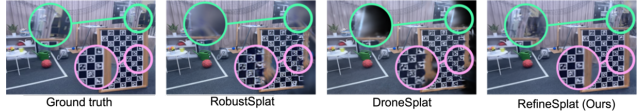


Figure 16. An analysis of sparsity issue on the Corner scene. visualize how the transient mask works, as illustrated in Fig. 28. Specifically, our Entropy-aware adaptive masking can capture more fine-grained details compared to prior methods. Moreover, we provide details of memory, as shown in Tab. 23.

Comparison on the Drone Imagery Dataset. We provide further qualitative and quantitative results, as shown in Fig. 24 and Tab. 19. While DroneSplat [46] shows impressive rendering quality, it struggles to capture ambiguous color similarities between static elements and distractors, as it relies on residual errors to generate invariant masks extracted from SAM [19] before training. Although RobustSplat [11] also shows great results, it only depends on semantic features to capture transient elements, which makes it hard to tackle similar semantic levels to static elements. In contrast, RefineSplat considers distractors at the instance level to better identify ambiguous distractors between transient and static elements. Moreover, we show the efficacy of our entropy-aware adaptive mask on the Drone Imagery dataset [46], as shown in Fig. 29.

E. Ablation studies

Robustness of adaptive entropy threshold. To demonstrate the robustness of the adaptive entropy threshold for variation of the entropy compared to baselines, we show step-by-step proof by differentiating \mathcal{T}_{ent} . The derivation for \mathcal{T}_{ent} can be calculated as:

$$\frac{\partial \mathcal{T}_{ent}}{\partial \mathcal{H}_i} \propto -w_2 \log(\mathcal{H}_i). \quad (16)$$

On the other hand, the derivation for $\mathcal{T}_{statistics}$, which is utilized in DroneSplat [46], is calculated as follows:

$$\frac{\partial \mathcal{T}_{statistics}}{\partial \mathcal{H}_i} \propto \frac{2}{N} (\mathcal{H}_i - \mu_{\mathcal{H}}). \quad (17)$$

Thus, compared to the derivation for $\mathcal{T}_{statistics}$, utilizing a logarithm to construct transient masks for capturing distractors, \mathcal{T}_{ent} is less sensitive to variation of a skew entropy distribution. Furthermore, we also observe that leveraging \mathcal{T}_{ent} constructs robust transient masks compared to baselines, as shown in Fig. 13. Note that, to focus on the core part of the derivation, we discard constant terms that emerge during the derivation.

Appearance variations on the Photo Tourism dataset. Furthermore, we examine whether RefineSplat addresses appearance variations and consistently maintains appearance, as illustrated in Fig. 17. To tackle appearance variations, we follow the appearance modeling strategy from



Figure 17. Visualization of Appearance variations on the Photo Tourism dataset.

WildGaussians[21], which utilizes per-view image embeddings to handle appearance variations with Adam optimizer [18]. The per-view image embeddings are of size 32. For the appearance MLP, we use 2 layers of size 128 with ReLU activations.

F. Future works

Future works. RefineSplat achieves superior results in capturing ambiguous distractors across diverse real-world datasets by leveraging entropy and instance masks. However, similar to existing approaches, our method struggles to generalize in 3D novel-view synthesis from unconstrained sparse training views in diverse real-world scenarios, as shown in Fig. 16. To address these issues, a feasible solution is to integrate our methods with diffusion models [38] to interpolate the sparsity region in the Gaussian field and distill a 3D representation. Moreover, while we demonstrate the effectiveness of RefineSplat on the Photo Tourism [45], Drone Imagery [46], NeRF On-the-go [37], and Ambiguous wild datasets, another promising direction is extending RefineSplat to large-scale dynamic scenes such as KITTI360 [27], NuScenes [3], and Cosmos [1]. Furthermore, since real-world scenarios often contain both blurring issues and diverse distractors, constructing such datasets would be a promising future direction to tackle extreme real-world scenarios. We leave this as future extension works.

Method	GPU hrs / FPS	Artwork			Benches			Bookstore			Jewel			Monster			Wood		
		PSNR↑	SSIM↑	LPIPS↓	PSNR↑	SSIM↑	LPIPS↓	PSNR↑	SSIM↑	LPIPS↓	PSNR↑	SSIM↑	LPIPS↓	PSNR↑	SSIM↑	LPIPS↓	PSNR↑	SSIM↑	LPIPS↓
3DGS [17]	1.8 / 57	27.13	0.943	0.202	26.64	0.903	0.113	20.66	0.688	0.251	25.62	0.899	0.105	20.43	0.856	0.136	17.14	0.766	0.369
Mip-Splatting [57]	1.75 / 66	28.42	0.954	0.185	27.65	0.913	0.102	22.24	0.734	0.231	26.07	0.905	0.099	20.37	0.872	0.129	17.88	0.795	0.344
GS-W [59]	1.01 / 106	31.15	0.963	0.151	25.67	0.837	0.123	20.40	0.552	0.461	26.68	0.882	0.106	21.14	0.893	0.085	18.99	0.889	0.295
WildGaussians [21]	1.63 / 102	27.22	0.943	0.197	23.68	0.794	0.193	19.59	0.457	0.585	25.21	0.849	0.152	20.91	0.855	0.147	18.42	0.844	0.326
NexusSplats [47]	1.31 / 98	24.58	0.933	0.241	23.08	0.789	0.218	19.81	0.509	0.474	25.88	0.862	0.146	21.03	0.866	0.142	18.35	0.794	0.415
DroneSplat [46]	0.71 / 104	31.44	0.958	0.032	26.14	0.869	0.083	22.40	0.695	0.202	26.69	0.889	0.066	20.68	0.861	0.094	19.72	0.818	0.203
RobustSplat [11]	0.41 / 106	31.79	0.961	0.207	25.37	0.83	0.234	21.20	0.529	0.472	26.78	0.885	0.154	21.78	0.890	0.119	21.20	0.887	0.236
RefineSplat (Ours)	0.54 / 105	32.45	0.975	0.138	28.06	0.915	0.106	23.24	0.743	0.228	27.88	0.919	0.089	22.20	0.911	0.086	22.68	0.902	0.197

Table 15. Quantitative result on the Ambiguous wild dataset. Performance is highlighted by color from third to first.

Method	GPU hrs / FPS	Room			Rose			Turtle			Siedentopf			Stone			Straw		
		PSNR↑	SSIM↑	LPIPS↓	PSNR↑	SSIM↑	LPIPS↓	PSNR↑	SSIM↑	LPIPS↓	PSNR↑	SSIM↑	LPIPS↓	PSNR↑	SSIM↑	LPIPS↓	PSNR↑	SSIM↑	LPIPS↓
3DGS [17]	1.9 / 61	20.47	0.824	0.205	23.19	0.818	0.195	22.84	0.842	0.144	18.82	0.803	0.237	28.36	0.935	0.108	22.84	0.842	0.144
Mip-Splatting [57]	1.61 / 73	21.24	0.837	0.214	23.75	0.824	0.192	22.85	0.793	0.189	20.45	0.834	0.205	29.91	0.693	0.316	21.23	0.863	0.129
GS-W [59]	1.02 / 104	22.22	0.902	0.134	24.10	0.758	0.240	20.56	0.679	0.299	19.62	0.844	0.228	32.49	0.962	0.076	23.23	0.763	0.173
WildGaussians [21]	1.47 / 101	21.37	0.852	0.192	20.71	0.734	0.293	19.62	0.601	0.412	21.01	0.826	0.254	32.01	0.959	0.077	23.87	0.809	0.135
NexusSplats [47]	1.19 / 96	21.59	0.848	0.219	22.61	0.731	0.326	20.24	0.633	0.341	20.32	0.828	0.235	30.41	0.935	0.129	20.82	0.706	0.270
DroneSplat [46]	1.67 / 101	22.42	0.850	0.144	24.17	0.801	0.123	22.49	0.752	0.155	23.42	0.866	0.096	30.97	0.946	0.054	24.17	0.830	0.107
RobustSplat [11]	0.37 / 104	22.89	0.890	0.179	24.21	0.749	0.344	21.32	0.656	0.350	22.97	0.859	0.247	32.091	0.948	0.136	23.195	0.752	0.260
RefineSplat (Ours)	0.45 / 107	23.24	0.911	0.123	25.73	0.847	0.182	23.65	0.804	0.182	25.11	0.914	0.132	34.16	0.975	0.069	25.58	0.878	0.116

Table 16. Quantitative result on the Ambiguous wild dataset. Performance is highlighted by color from third to first.

Method	GPU hrs / FPS	Mountain			Fountain			Corner			Patio			Spot			Patio-High		
		PSNR↑	SSIM↑	LPIPS↓	PSNR↑	SSIM↑	LPIPS↓	PSNR↑	SSIM↑	LPIPS↓	PSNR↑	SSIM↑	LPIPS↓	PSNR↑	SSIM↑	LPIPS↓	PSNR↑	SSIM↑	LPIPS↓
Ha-NeRF [34]	- / <1	18.64	0.485	0.499	16.71	0.393	0.569	19.23	0.684	0.367	16.82	0.543	0.393	17.85	0.460	0.599	16.67	0.463	0.505
3DGS [17]	0.35 / 116	19.40	0.638	0.213	19.96	0.659	0.185	20.90	0.713	0.241	17.48	0.704	0.199	20.77	0.693	0.316	17.29	0.604	0.363
Mip-Splatting [57]	0.18 / 82	19.23	0.581	0.273	19.74	0.624	0.252	21.44	0.767	0.161	16.96	0.688	0.188	21.14	0.757	0.220	19.12	0.640	0.303
Splatfacto-W [52]	1.03 / 43.1	20.70	0.661	0.169	20.37	0.662	0.187	21.53	0.739	0.241	15.58	0.491	0.536	20.03	0.683	0.324	15.58	0.491	0.536
GS-W [59]	1.03 / 105	19.43	0.596	0.299	20.06	0.723	0.274	22.17	0.793	0.155	19.90	0.681	0.260	17.13	0.608	0.409	19.90	0.681	0.260
WildGaussian [21]	1.56 / 94	20.43	0.653	0.255	20.81	0.662	0.215	24.16	0.822	0.045	21.44	0.800	0.138	23.82	0.816	0.138	22.23	0.725	0.206
SpotLessSplats [40]	1.87 / 81	19.84	0.580	0.294	20.19	0.612	0.258	24.03	0.795	0.258	21.55	0.838	0.065	23.52	0.756	0.185	20.31	0.664	0.259
DeSplat [49]	0.84 / 106	19.59	0.710	0.170	20.27	0.680	0.170	26.05	0.880	0.090	20.89	0.810	0.110	26.07	0.900	0.090	22.59	0.840	0.120
HybridGS [28]	0.98 / 112	21.73	0.693	0.284	21.11	0.674	0.252	25.03	0.847	0.151	21.98	0.812	0.169	24.33	0.794	0.196	21.77	0.741	0.211
DroneSplat [46]	1.35 / 101	21.23	0.687	0.162	21.54	0.705	0.168	24.77	0.823	0.106	21.85	0.816	0.107	24.37	0.821	0.095	22.53	0.778	0.181
RobustSplat [11]	0.75 / 116	21.15	0.737	0.201	21.01	0.701	0.207	25.88	0.876	0.144	21.63	0.827	0.139	24.85	0.808	0.164	21.84	0.757	0.192
T-3DGS [31]	1.72 / 103	20.62	0.703	0.223	20.83	0.681	0.218	26.14	0.890	0.114	20.96	0.819	0.154	25.84	0.893	0.127	22.76	0.831	0.170
RefineSplat (Ours)	0.93 / 115	22.62	0.772	0.167	21.51	0.732	0.188	26.42	0.897	0.104	22.08	0.831	0.126	25.87	0.869	0.142	22.71	0.841	0.159

Table 17. Quantitative result on the NeRF On-the-go dataset. Performance is highlighted by color from third to first.

Method	GPU hrs / FPS	Brandenburg Gate			Sacre Coeur			Trevi-Fountain		
		PSNR↑	SSIM↑	LPIPS↓	PSNR↑	SSIM↑	LPIPS↓	PSNR↑	SSIM↑	LPIPS↓
Ha-NeRF [34]	452 / <1	24.04	0.877	0.139	20.02	0.801	0.171	20.18	0.690	0.222
3DGS [17]	2.2 / 57	19.33	0.884	0.132	17.70	0.845	0.176	17.08	0.714	0.241
Mip-Splatting [57]	0.18 / 82	20.46	0.890	0.126	18.14	0.879	0.168	17.52	0.747	0.218
Splatfacto-W [52]	1.05 / 40.2	26.82	0.911	0.126	22.56	0.876	0.157	22.28	0.766	0.235
GS-W [59]	1.2 / 51	23.51	0.897	0.166	19.39	0.825	0.211	20.06	0.723	0.271
WildGaussian [21]	11.5 / 86	27.77	0.927	0.133	22.56	0.859	0.177	23.63	0.766	0.228
SWAG [9]	0.8 / 15	26.33	0.929	0.139	21.16	0.860	0.185	23.10	0.815	0.208
NexusSplats [47]	6.81 / 88	27.12	0.924	0.143	22.61	0.857	0.180	23.92	0.761	0.253
DroneSplat [46]	1.8 / 97	19.88	0.871	0.112	16.85	0.808	0.143	16.71	0.661	0.276
RobustSplat [11]	1.01 / 103	19.74	0.887	0.146	17.87	0.847	0.178	17.63	0.623	0.727
ForestSplats [36]	7.9 / 122	28.13	0.935	0.118	23.84	0.876	0.123	23.11	0.802	0.212
RefineSplat (Ours)	2.13 / 109	27.81	0.929	0.117	24.16	0.889	0.137	23.71	0.792	0.204

Table 18. Quantitative result on the Photo Tourism dataset. Performance is highlighted by color from third to first.

Method	GPU hrs / FPS	SimingShan			Sculpture		
		PSNR \uparrow	SSIM \uparrow	LPIPS \downarrow	PSNR \uparrow	SSIM \uparrow	LPIPS \downarrow
3DGS [17]	1.1 / 59	18.14	0.749	0.317	16.11	0.396	0.286
Mip-Splatting [57]	0.8 / 63	19.78	0.742	0.295	17.22	0.404	0.249
Ha-NeRF [34]	32 / < 1	22.26	0.767	0.298	18.35	0.412	0.274
Splatfacto-W [52]	0.6 / 71	22.13	0.715	0.268	17.49	0.438	0.289
GS-W [59]	0.6 / 104	22.41	0.706	0.243	17.34	0.414	0.271
WildGaussian [21]	1.3 / 94	22.63	0.707	0.239	17.15	0.371	0.383
DroneSplat [46]	1.5 / 104	23.16	0.759	0.152	18.48	0.489	0.225
RobustSplat [11]	0.57 / 109	23.20	0.703	0.476	19.14	0.447	0.461
RefineSplat (Ours)	0.72 / 111	24.08	0.801	0.226	19.64	0.515	0.299

Table 19. Quantitative result on the Drone Imagery dataset. Performance is highlighted by color from third to first.

Method	Porter	Humanoid	Jockey	Lounge	Monster	Artwork	Benches	Bust	Statuette
3DGS [17]	447.08	413.04	396.69	247.98	277.27	103.08	380.86	472.09	370.94
Mip-Splatting [57]	521.56	213.16	412.77	203.82	194.96	54.24	432.05	465.87	357.62
DroneSplat [46]	389.84	110.01	288.72	114.13	79.24	22.12	269.96	294.58	266.31
RobustSplat [11]	347.45	51.32	214.27	86.68	64.39	62.03	266.12	226.19	211.20
RefineSplat (Ours)	306.91	43.24	165.83	85.13	25.80	20.31	227.64	187.64	193.71

Table 20. Comparison of memory efficiency on the Ambiguous wild dataset.

Method	Bookstore	Room	Rose	Turtle	Sidentopf	Wood	Stone	Straw	Jewel
3DGS [17]	348.39	243.30	276.89	311.95	331.80	145.98	152.18	550.00	247.71
Mip-Splatting [57]	327.32	173.06	325.42	371.53	225.57	174.80	79.83	595.35	274.48
DroneSplat [46]	249.59	107.08	231.89	245.38	108.92	117.45	91.45	394.02	176.21
RobustSplat [11]	295.95	104.01	205.61	220.56	84.70	108.19	31.54	377.40	166.67
RefineSplat (Ours)	263.56	97.70	197.57	203.87	79.37	102.69	29.68	336.50	153.37

Table 21. Comparison of memory size on the Ambiguous wild dataset.

Method	Mountain	Fountain	Corner	Patio	Spot	Patio-High
3DGS [17]	447.08	413.04	396.69	247.98	277.27	103.08
Mip-Splatting [57]	521.56	213.16	412.77	203.82	194.96	54.24
DroneSplat [46]	389.84	110.01	288.72	114.13	79.24	22.12
RobustSplat [11]	347.45	51.32	214.27	86.68	64.39	62.03
RefineSplat (Ours)	306.91	46.85	218.63	86.61	25.80	20.31

Table 22. Comparison of memory efficiency on the NeRF On-the-go dataset.

Method	Photo Tourism		
	Brandenburg Gate	Sacre Coeur	Trevi-Fountain
WildGaussians [21]	60.50	69.35	151.39
DroneSplat [46]	54.11	77.12	127.16
RobustSplat [11]	82.29	82.15	183.13
RefineSplat (Ours)	37.51	31.26	108.84

Table 23. Comparison of memory efficiency on the Photo Tourism dataset.



Figure 18. Additional sample images on the Ambiguous wild dataset.



Figure 19. Additional sample images on the Ambiguous wild dataset.

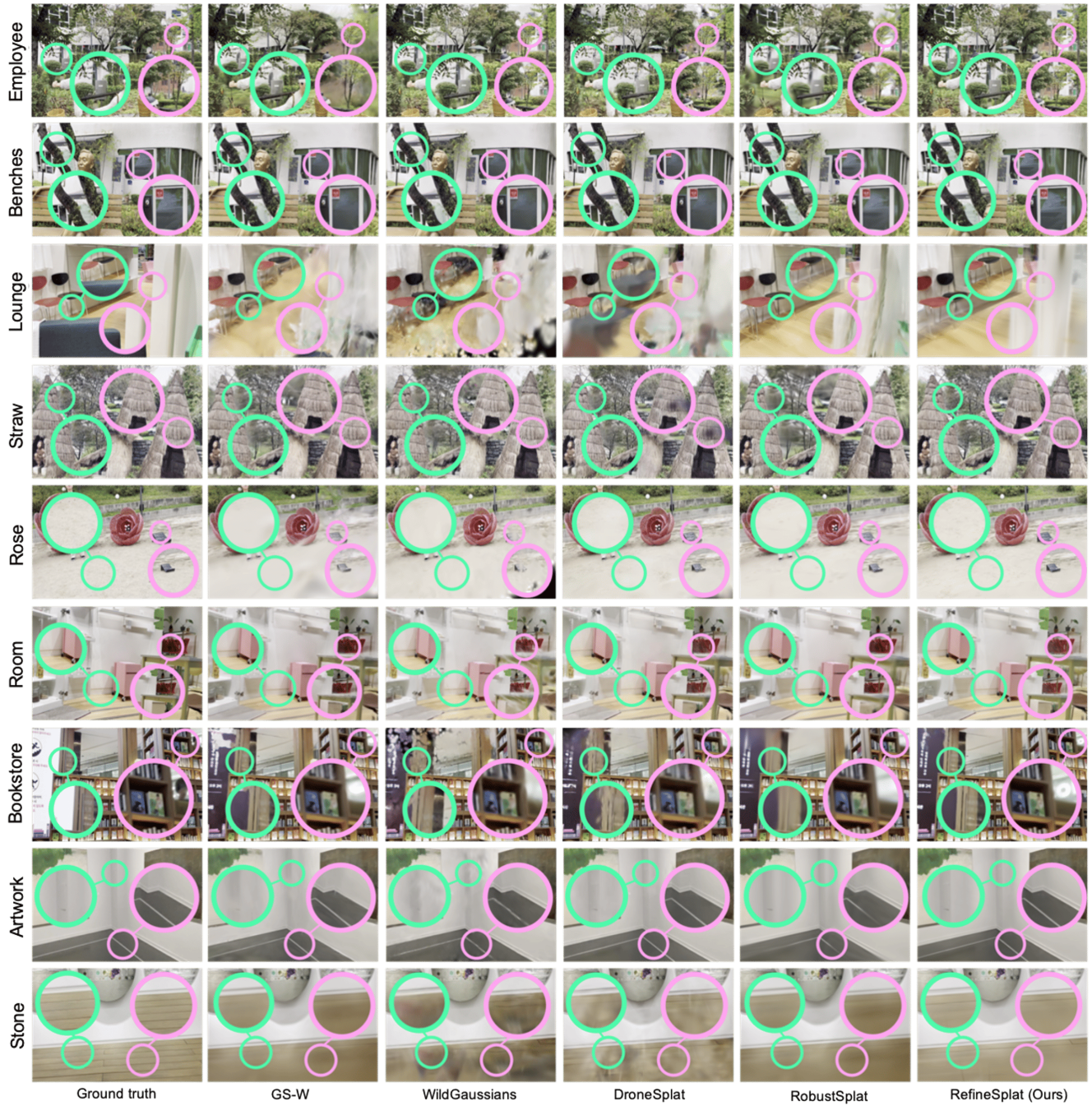


Figure 20. Additional qualitative results on the Ambiguous wild dataset.



Figure 21. Additional qualitative results on the Ambiguous wild dataset.

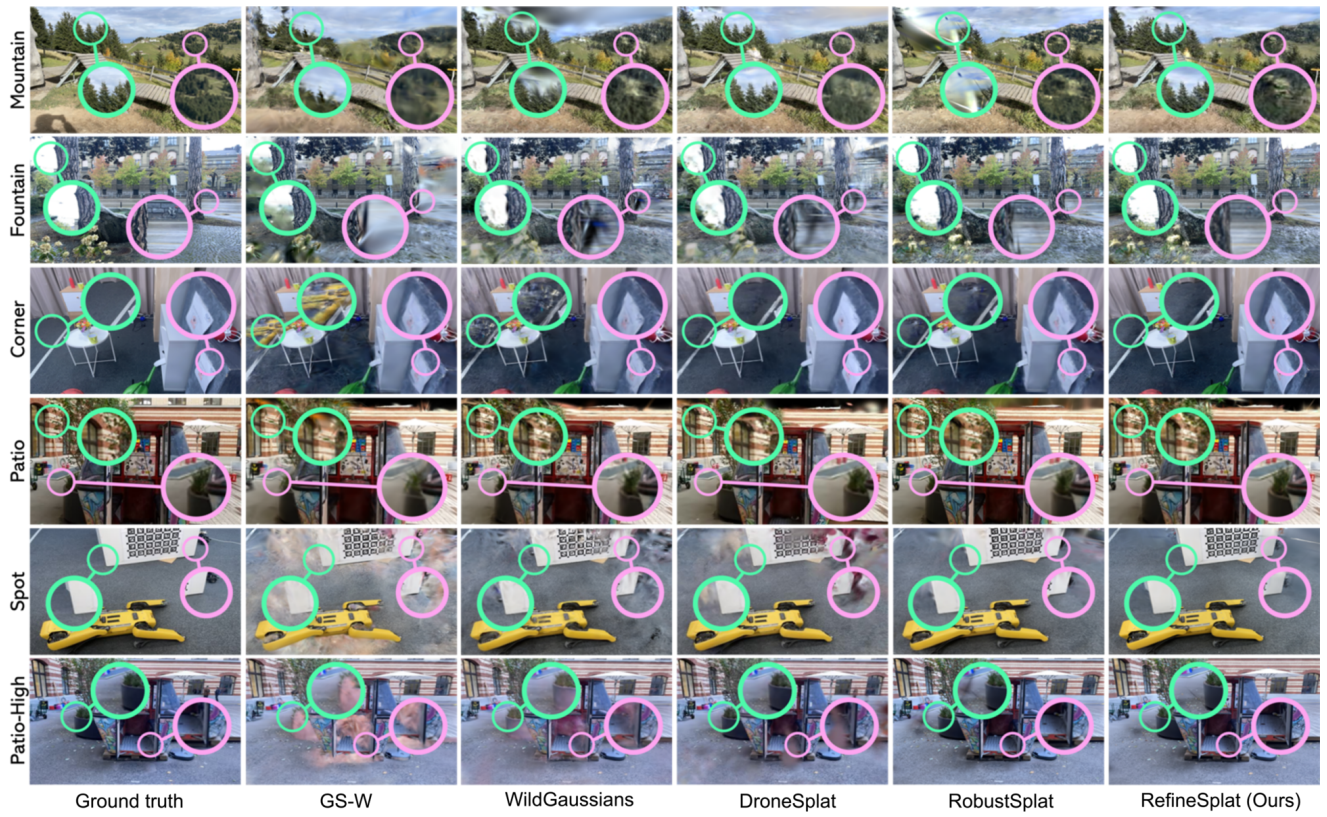


Figure 22. Additional qualitative results on the NeRF On-the-go dataset.



Figure 23. Additional qualitative results on the Photo Tourism dataset.

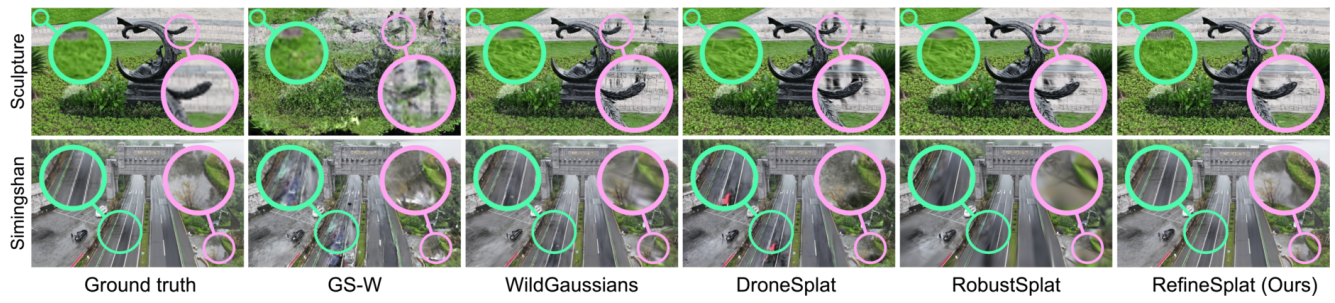


Figure 24. Additional qualitative results on the DroneSplat dataset.



Figure 25. Comparison of transient masks in the Ambiguous wild dataset.

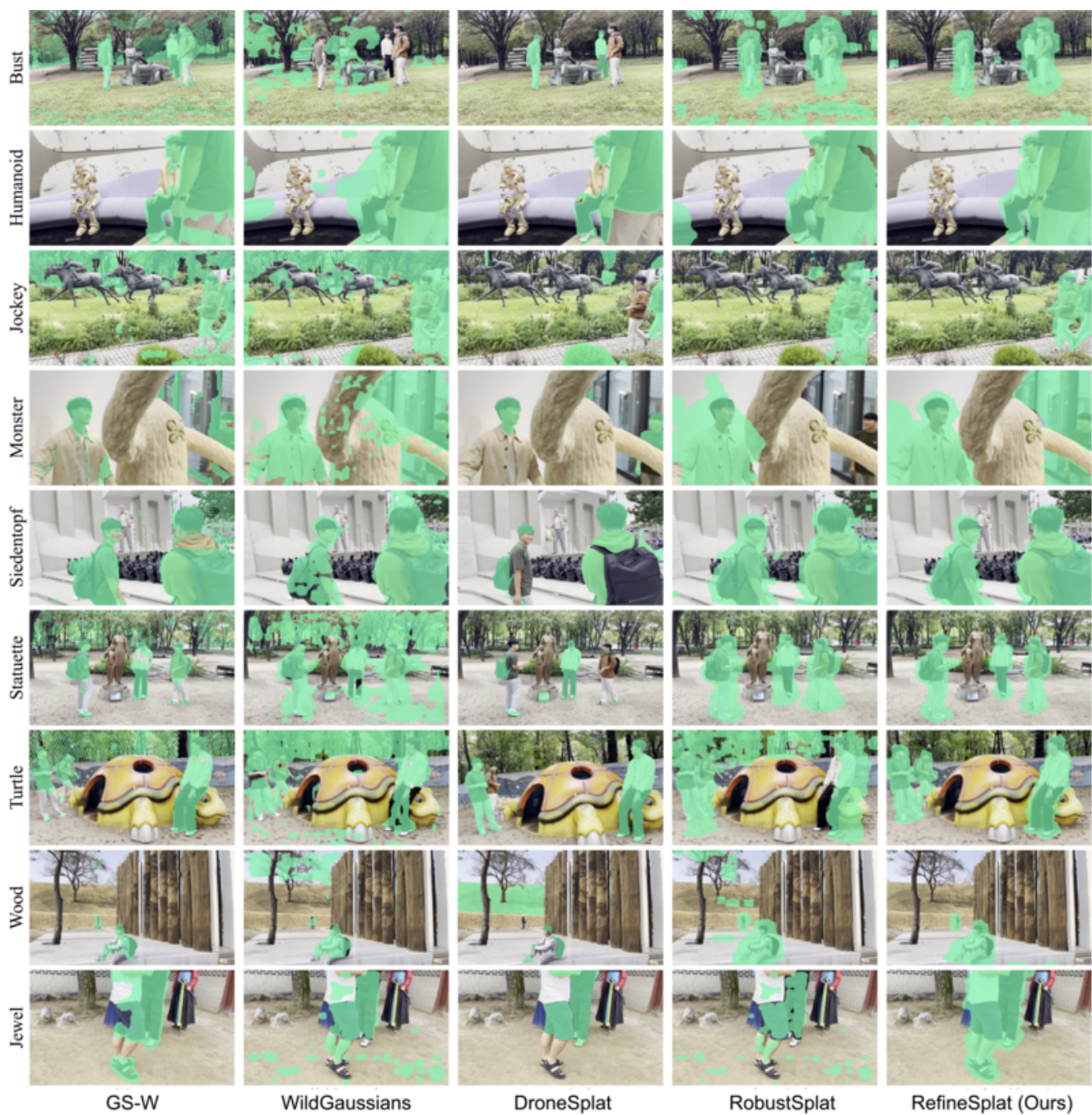


Figure 26. Comparison of transient masks in the Ambiguous wild dataset.



Figure 27. Comparison of transient masks in the NeRF On-the-go dataset.

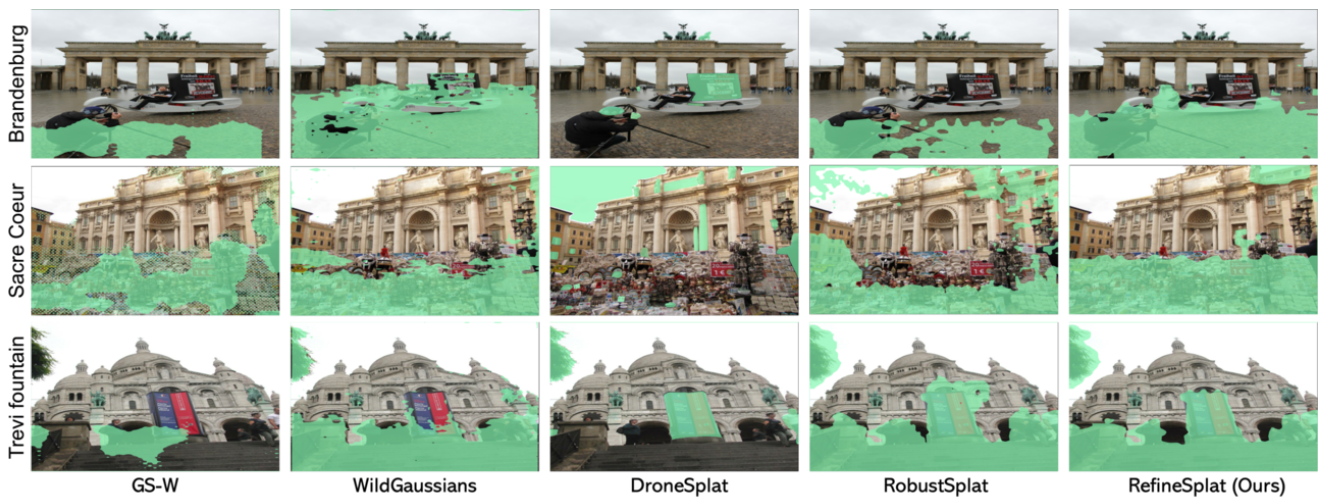


Figure 28. Comparison of transient masks in the Photo Tourism dataset.

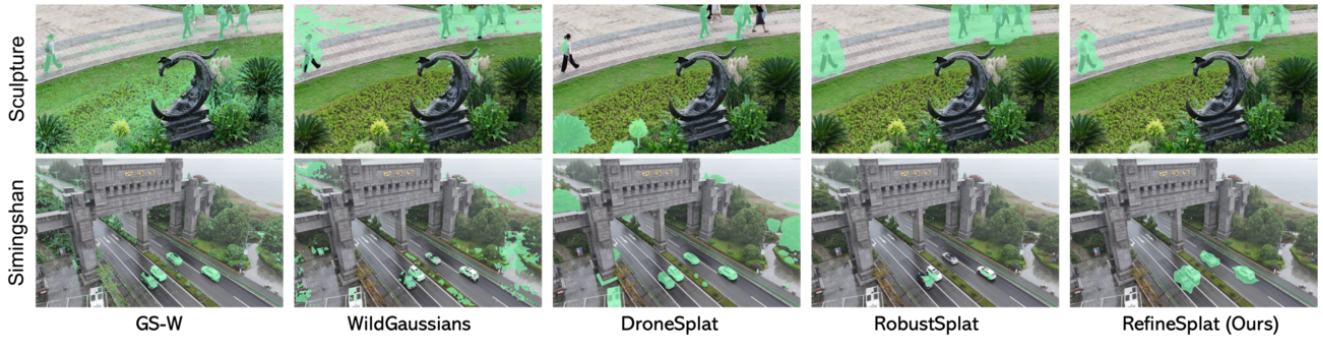



Figure 29. Comparison of transient masks in the Drone Imagery dataset.

Section A: Color/Background Ambiguity


Could an AI system confuse the object with its background due to similar color or texture?
Select "Yes" if confusion seems possible, "No" if not.

Q1



Yes
 No


Q2




Yes
 No

Section B: Semantic Similarity Ambiguity

Could an AI system confuse the statue or mannequin with a human?
Select "Yes" if confusion seems possible, "No" if not.



Yes
 No



Yes
 No

Figure 30. Our user study questionnaire. Each participant was shown an upper figure, which is a rendering video of several scenes using different methods. After watching the video, they were asked to answer the question below.

Notation	Shape	Definition
μ	\mathbb{R}^3	Position of 3D Gaussians
Σ	$\mathbb{R}^{3 \times 3}$	Covariance matrix of 3D Gaussians
S	$S_k \in \mathbb{R}^3$	Scaling matrix of Gaussians
R	$R_k \in \text{SO}(3)$	Rotation matrix of Gaussians
α	\mathbb{R}^1	Opacity of 3D Gaussians
c	\mathbb{R}^3	View-dependent color of 3D Gaussians
W	$\mathbb{R}^{3 \times 3}$	Viewing transformation matrix
J	$\mathbb{R}^{2 \times 3}$	Jacobian of the affine approximation of the projective transformation
C	\mathbb{R}^3	The obtained pixel value of the rendered image
\hat{I}	$\mathbb{R}^{3 \times H \times W}$	Rendered image
I_{gt}	$\mathbb{R}^{3 \times H \times W}$	Ground truth image
N_{sh}		Spherical harmonics (SH) coefficients
\mathcal{M}_{global}	$\mathbb{R}^{H \times W}$	Entropy-aware global mask
\mathcal{M}_{local}	$\mathbb{R}^{H \times W}$	Entropy-aware local mask
\mathcal{M}_{final}	$\mathbb{R}^{H \times W}$	Entropy-aware adaptive mask
$\mathcal{B}_{3 \times 3}$		Box filter
\mathcal{D}_θ		DINO feature extractor
\mathcal{T}_{ent}		Adaptive entropy threshold
$\mathcal{T}_{statistics}$		Dynamic Threshold for the transient mask of DroneSplat
\mathcal{T}_{hard}		Fixed value Threshold
\mathcal{T}_{over}		Overlap Ratio
ψ_θ		MLP Layer
\mathcal{H}_i		Entropy
$\mathcal{E}()$		Shannon Entropy function
\mathcal{E}_i		Confidence for instances
ψ_θ		MLP Layer
$(\mu_k^*, c_k^*, \alpha_k^*, \Sigma_k^*)$		The new attributes of merged Gaussians

Table 24. For clarity and to avoid confusion in notation, we provided notation table to easily understand our method.

References

- [1] Niket Agarwal, Arslan Ali, Maciej Bala, Yogesh Balaji, Erik Barker, Tiffany Cai, Prithvijit Chattopadhyay, Yongxin Chen, Yin Cui, Yifan Ding, et al. Cosmos world foundation model platform for physical ai. *arXiv preprint arXiv:2501.03575*, 2025. 4
- [2] Samuel Rota Bulò, Lorenzo Porzi, and Peter Kontschieder. Revising densification in gaussian splatting. *arXiv preprint arXiv:2404.06109*, 2024. 3, 1
- [3] Holger Caesar, Varun Bankiti, Alex H Lang, Sourabh Vora, Venice Erin Liong, Qiang Xu, Anush Krishnan, Yu Pan, Giancarlo Baldan, and Oscar Beijbom. nuscenes: A multi-modal dataset for autonomous driving. In *Proceedings of the IEEE/CVF conference on computer vision and pattern recognition*, pages 11621–11631, 2020. 4
- [4] Jiahao Chen, Yipeng Qin, Lingjie Liu, Jiangbo Lu, and Guanbin Li. Nerf-hugs: Improved neural radiance fields in non-static scenes using heuristics-guided segmentation. In *Proceedings of the IEEE/CVF Conference on Computer Vision and Pattern Recognition*, pages 19436–19446, 2024. 1
- [5] Xingyu Chen, Qi Zhang, Xiaoyu Li, Yue Chen, Ying Feng, Xuan Wang, and Jue Wang. Hallucinated neural radiance fields in the wild. In *Proceedings of the IEEE/CVF Conference on Computer Vision and Pattern Recognition*, pages 12943–12952, 2022. 6, 7
- [6] Yihang Chen, Qianyi Wu, Weiyao Lin, Mehrtaash Harandi, and Jianfei Cai. Hac: Hash-grid assisted context for 3d gaussian splatting compression. In *European Conference on Computer Vision*, pages 422–438. Springer, 2024. 3
- [7] Ho Kei Cheng, Seoung Wug Oh, Brian Price, Alexander Schwing, and Joon-Young Lee. Tracking anything with decoupled video segmentation. In *Proceedings of the IEEE/CVF International Conference on Computer Vision*, pages 1316–1326, 2023. 3, 6, 1, 2
- [8] Kai Cheng, Xiaoxiao Long, Kaizhi Yang, Yao Yao, Wei Yin, Yuexin Ma, Wenping Wang, and Xuejin Chen. Gaussianpro: 3d gaussian splatting with progressive propagation. In *Forty-first International Conference on Machine Learning*, 2024. 1
- [9] Hiba Dahmani, Moussab Bennehar, Nathan Piasco, Luis Roldao, and Dzmitry Tsishkou. Swag: Splatting in the wild images with appearance-conditioned gaussians. In *European Conference on Computer Vision*, pages 325–340. Springer, 2024. 2, 3, 5
- [10] Zhiwen Fan, Kevin Wang, Kairun Wen, Zehao Zhu, De-jia Xu, and Zhangyang Wang. Lightgaussian: Unbounded 3d gaussian compression with 15x reduction and 200+ fps. *arXiv preprint arXiv:2311.17245*, 2023. 3
- [11] Chuanyu Fu, Yuqi Zhang, Kunbin Yao, Guanying Chen, Yuan Xiong, Chuan Huang, Shuguang Cui, and Xiaochun Cao. Robustsplat: Decoupling densification and dynamics for transient-free 3dgs. *arXiv preprint arXiv:2506.02751*, 2025. 1, 2, 4, 5, 6, 7, 8, 3
- [12] Zihui Gao, Jia-Wang Bian, Guosheng Lin, Hao Chen, and Chunhua Shen. Surfacesplat: Connecting surface reconstruction and gaussian splatting. In *Proceedings of the IEEE/CVF International Conference on Computer Vision*, pages 28525–28534, 2025. 2
- [13] Alex Hanson, Allen Tu, Vasu Singla, Mayuka Jayawardhana, Matthias Zwicker, and Tom Goldstein. Pup 3d-gs: Principled uncertainty pruning for 3d gaussian splatting. In *Proceedings of the Computer Vision and Pattern Recognition Conference*, pages 5949–5958, 2025. 7
- [14] Wenbo Hu, Yuling Wang, Lin Ma, Bangbang Yang, Lin Gao, Xiao Liu, and Yuewen Ma. Tri-miprf: Tri-mip representation for efficient anti-aliasing neural radiance fields. In *Proceedings of the IEEE/CVF International Conference on Computer Vision*, pages 19774–19783, 2023. 1
- [15] Letian Huang, Jie Guo, Jialin Dan, Ruoyu Fu, Yuanqi Li, and Yanwen Guo. Spectral-gs: Taming 3d gaussian splatting with spectral entropy. In *Proceedings of the SIGGRAPH Asia 2025 Conference Papers*, pages 1–11, 2025. 1
- [16] Yuheng Jiang, Zhehao Shen, Yu Hong, Chengcheng Guo, Yize Wu, Yingliang Zhang, Jingyi Yu, and Lan Xu. Robust dual gaussian splatting for immersive human-centric volumetric videos. *ACM Transactions on Graphics (TOG)*, 43(6):1–15, 2024. 3
- [17] Bernhard Kerbl, Georgios Kopanas, Thomas Leimkühler, and George Drettakis. 3d gaussian splatting for real-time radiance field rendering. *ACM Trans. Graph.*, 42(4):139–1, 2023. 1, 2, 3, 6, 7, 5
- [18] Diederik P Kingma. Adam: A method for stochastic optimization. *arXiv preprint arXiv:1412.6980*, 2014. 6, 2, 4
- [19] Alexander Kirillov, Eric Mintun, Nikhila Ravi, Hanzi Mao, Chloe Rolland, Laura Gustafson, Tete Xiao, Spencer Whitehead, Alexander C Berg, Wan-Yen Lo, et al. Segment anything. In *Proceedings of the IEEE/CVF international conference on computer vision*, pages 4015–4026, 2023. 2, 4, 7, 3
- [20] Jonas Kulhanek and Torsten Sattler. Nerfbaselines: Consistent and reproducible evaluation of novel view synthesis methods. *arXiv preprint arXiv:2406.17345*, 2024. 2
- [21] Jonas Kulhanek, Songyou Peng, Zuzana Kukelova, Marc Pollefeys, and Torsten Sattler. Wildgaussians: 3d gaussian splatting in the wild. *arXiv preprint arXiv:2407.08447*, 2024. 1, 2, 4, 5, 6, 7, 3
- [22] Joo Chan Lee, Daniel Rho, Xiangyu Sun, Jong Hwan Ko, and Eunbyung Park. Compact 3d gaussian representation for radiance field. In *Proceedings of the IEEE/CVF Conference on Computer Vision and Pattern Recognition*, pages 21719–21728, 2024. 3, 1
- [23] Joo Chan Lee, Jong Hwan Ko, and Eunbyung Park. Optimized minimal 3d gaussian splatting. *arXiv preprint arXiv:2503.16924*, 2025. 3
- [24] Chengqi Li, Zhihao Shi, Yangdi Lu, Wenbo He, and Xiangyu Xu. Robust neural rendering in the wild with asymmetric dual 3d gaussian splatting. *Advances in Neural Information Processing Systems*, 38:50166–50191, 2026. 5
- [25] Peihao Li, Shaohui Wang, Chen Yang, Bingbing Liu, Weichao Qiu, and Haoqian Wang. Nerf-ms: Neural radiance fields with multi-sequence. In *Proceedings of the IEEE/CVF International Conference on Computer Vision*, pages 18591–18600, 2023. 1, 2
- [26] Yue Li, Qi Ma, Runyi Yang, Huapeng Li, Mengjiao Ma, Bin Ren, Nikola Popovic, Nicu Sebe, Ender Konukoglu, Theo

- Gevers, et al. Scenesplat: Gaussian splatting-based scene understanding with vision-language pretraining. *arXiv preprint arXiv:2503.18052*, 2025. 2
- [27] Yiyi Liao, Jun Xie, and Andreas Geiger. Kitti-360: A novel dataset and benchmarks for urban scene understanding in 2d and 3d. *IEEE Transactions on Pattern Analysis and Machine Intelligence*, 45(3):3292–3310, 2022. 4
- [28] Jingyu Lin, Jiaqi Gu, Lubin Fan, Bojian Wu, Yujing Lou, Renjie Chen, Ligang Liu, and Jieping Ye. Hybrids: Decoupling transients and statics with 2d and 3d gaussian splatting. *arXiv preprint arXiv:2412.03844*, 2024. 2, 3, 5
- [29] Tao Lu, Mulin Yu, Linning Xu, Yuanbo Xiangli, Limin Wang, Dahua Lin, and Bo Dai. Scaffold-gs: Structured 3d gaussians for view-adaptive rendering. In *Proceedings of the IEEE/CVF Conference on Computer Vision and Pattern Recognition*, pages 20654–20664, 2024. 3
- [30] Saswat Subhajyoti Mallick, Rahul Goel, Bernhard Kerbl, Markus Steinberger, Francisco Vicente Carrasco, and Fernando De La Torre. Taming 3dgs: High-quality radiance fields with limited resources. In *SIGGRAPH Asia 2024 Conference Papers*, pages 1–11, 2024. 1
- [31] Alexander Markin, Vadim Pryadilshchikov, Artem Komarichev, Ruslan Rakhimov, Peter Wonka, and Evgeny Burnaev. T-3dgs: Removing transient objects for 3d scene reconstruction. *arXiv preprint arXiv:2412.00155*, 2024. 1, 2, 5
- [32] Ricardo Martin-Brualla, Noha Radwan, Mehdi SM Sajjadi, Jonathan T Barron, Alexey Dosovitskiy, and Daniel Duckworth. Nerf in the wild: Neural radiance fields for unconstrained photo collections. In *Proceedings of the IEEE/CVF conference on computer vision and pattern recognition*, pages 7210–7219, 2021. 1, 2
- [33] Xuyi Meng, Chen Wang, Jiahui Lei, Kostas Daniilidis, Jiatuo Gu, and Lingjie Liu. Zero-1-to-g: Taming pretrained 2d diffusion model for direct 3d generation. *arXiv preprint arXiv:2501.05427*, 2025. 5
- [34] Ben Mildenhall, Pratul P Srinivasan, Matthew Tancik, Jonathan T Barron, Ravi Ramamoorthi, and Ren Ng. Nerf: Representing scenes as neural radiance fields for view synthesis. *Communications of the ACM*, 65(1):99–106, 2021. 1, 2, 3, 5, 6
- [35] Maxime Oquab, Timothée Darcet, Théo Moutakanni, Huy Vo, Marc Szafraniec, Vasil Khalidov, Pierre Fernandez, Daniel Haziza, Francisco Massa, Alaaeldin El-Nouby, et al. Dinov2: Learning robust visual features without supervision. *arXiv preprint arXiv:2304.07193*, 2023. 1, 2, 6
- [36] Wongi Park, Myeongseok Nam, Siwon Kim, Sangwoo Jo, and Soomok Lee. Forestsplats: Deformable transient field for gaussian splatting in the wild. In *Proceedings of the IEEE/CVF Winter Conference on Applications of Computer Vision*, pages 6978–6987, 2026. 1, 2, 3, 4, 7, 5
- [37] Weining Ren, Zihan Zhu, Boyang Sun, Jiaqi Chen, Marc Pollefeys, and Songyou Peng. Nerf on-the-go: Exploiting uncertainty for distractor-free nerfs in the wild. In *Proceedings of the IEEE/CVF Conference on Computer Vision and Pattern Recognition*, pages 8931–8940, 2024. 1, 2, 4, 6, 3
- [38] Robin Rombach, Andreas Blattmann, Dominik Lorenz, Patrick Esser, and Björn Ommer. High-resolution image synthesis with latent diffusion models. In *Proceedings of the IEEE/CVF conference on computer vision and pattern recognition*, pages 10684–10695, 2022. 3, 4
- [39] Sara Sabour, Suhani Vora, Daniel Duckworth, Ivan Krasin, David J Fleet, and Andrea Tagliasacchi. Robustnerf: Ignoring distractors with robust losses. In *Proceedings of the IEEE/CVF Conference on Computer Vision and Pattern Recognition*, pages 20626–20636, 2023. 1, 7
- [40] Sara Sabour, Lily Goli, George Kopanas, Mark Matthews, Dmitry Lagun, Leonidas Guibas, Alec Jacobson, David J Fleet, and Andrea Tagliasacchi. Spotlessplats: Ignoring distractors in 3d gaussian splatting. *arXiv preprint arXiv:2406.20055*, 2024. 1, 2, 4, 7, 3, 5
- [41] Johannes L Schonberger and Jan-Michael Frahm. Structure-from-motion revisited. In *Proceedings of the IEEE conference on computer vision and pattern recognition*, pages 4104–4113, 2016. 8, 2
- [42] Johannes Lutz Schönberger, Enliang Zheng, Marc Pollefeys, and Jan-Michael Frahm. Pixelwise View Selection for Unstructured Multi-View Stereo. In *European Conference on Computer Vision (ECCV)*, 2016. 3
- [43] Claude E Shannon. A mathematical theory of communication. *The Bell system technical journal*, 27(3):379–423, 1948. 4, 2
- [44] Seungjoo Shin, Jaesik Park, and Sunghyun Cho. Locality-aware gaussian compression for fast and high-quality rendering. *arXiv preprint arXiv:2501.05757*, 2025. 2
- [45] Noah Snavely, Steven M Seitz, and Richard Szeliski. Photo tourism: exploring photo collections in 3d. In *ACM siggraph 2006 papers*, pages 835–846. ACM, 2006. 6, 3, 4
- [46] Jiadong Tang, Yu Gao, Dianyi Yang, Liqi Yan, Yufeng Yue, and Yi Yang. Dronesplat: 3d gaussian splatting for robust 3d reconstruction from in-the-wild drone imagery. In *Proceedings of the Computer Vision and Pattern Recognition Conference*, pages 833–843, 2025. 1, 2, 4, 5, 6, 7, 3
- [47] Yuzhou Tang, Dejun Xu, Yongjie Hou, Zhenzhong Wang, and Min Jiang. Nexussplats: Efficient 3d gaussian splatting in the wild. *arXiv preprint arXiv:2411.14514*, 2024. 5, 7, 3
- [48] Peihao Wang, Yuehao Wang, Dilin Wang, Sreyas Mohan, Zhiwen Fan, Lemeng Wu, Ruisi Cai, Yu-Ying Yeh, Zhangyang Wang, Qiang Liu, et al. Steepest descent density control for compact 3d gaussian splatting. In *Proceedings of the Computer Vision and Pattern Recognition Conference*, pages 26663–26672, 2025. 3
- [49] Yihao Wang, Marcus Klasson, Matias Turkulainen, Shuzhe Wang, Juho Kannala, and Arno Solin. Desplat: Decomposed gaussian splatting for distractor-free rendering. *arXiv preprint arXiv:2411.19756*, 2024. 2, 3, 5
- [50] Yihao Wang, Marcus Klasson, Matias Turkulainen, Shuzhe Wang, Juho Kannala, and Arno Solin. Desplat: Decomposed gaussian splatting for distractor-free rendering. In *Proceedings of the Computer Vision and Pattern Recognition Conference*, pages 722–732, 2025. 2, 4
- [51] Zhou Wang, Alan C Bovik, Hamid R Sheikh, and Eero P Simoncelli. Image quality assessment: from error visibility to structural similarity. *IEEE TIP*, 13(4):600–612, 2004. 6
- [52] Congrong Xu, Justin Kerr, and Angjoo Kanazawa. Splatfacto-w: A nerfstudio implementation of gaussian

- splatting for unconstrained photo collections. *arXiv preprint arXiv:2407.12306*, 2024. [6](#), [7](#), [5](#)
- [53] Jiacong Xu, Yiqun Mei, and Vishal M Patel. Wild-gs: Real-time novel view synthesis from unconstrained photo collections. *arXiv preprint arXiv:2406.10373*, 2024. [2](#)
- [54] Lihe Yang, Bingyi Kang, Zilong Huang, Xiaogang Xu, Jiashi Feng, and Hengshuang Zhao. Depth anything: Unleashing the power of large-scale unlabeled data. In *Proceedings of the IEEE/CVF Conference on Computer Vision and Pattern Recognition*, pages 10371–10381, 2024. [2](#)
- [55] Yifan Yang, Shuhai Zhang, Zixiong Huang, Yubing Zhang, and Mingkui Tan. Cross-ray neural radiance fields for novel-view synthesis from unconstrained image collections. In *Proceedings of the IEEE/CVF International Conference on Computer Vision*, pages 15901–15911, 2023. [2](#), [1](#)
- [56] Zongxin Ye, Wenyu Li, Sidun Liu, Peng Qiao, and Yong Dou. Absgs: Recovering fine details in 3d gaussian splatting. In *Proceedings of the 32nd ACM International Conference on Multimedia*, pages 1053–1061, 2024. [3](#)
- [57] Zehao Yu, Anpei Chen, Binbin Huang, Torsten Sattler, and Andreas Geiger. Mip-splatting: Alias-free 3d gaussian splatting. In *Proceedings of the IEEE/CVF Conference on Computer Vision and Pattern Recognition*, pages 19447–19456, 2024. [1](#), [3](#), [5](#), [6](#), [7](#)
- [58] Zhaojie Zeng, Yuesong Wang, Lili Ju, and Tao Guan. Frequency-aware density control via reparameterization for high-quality rendering of 3d gaussian splatting. In *Proceedings of the AAAI Conference on Artificial Intelligence*, pages 9833–9841, 2025. [3](#)
- [59] Dongbin Zhang, Chuming Wang, Weitao Wang, Peihao Li, Minghan Qin, and Haoqian Wang. Gaussian in the wild: 3d gaussian splatting for unconstrained image collections. In *European Conference on Computer Vision*, pages 341–359. Springer, 2024. [1](#), [5](#), [6](#), [7](#), [3](#)
- [60] Richard Zhang, Phillip Isola, Alexei A Efros, Eli Shechtman, and Oliver Wang. The unreasonable effectiveness of deep features as a perceptual metric. In *Proceedings of the IEEE conference on computer vision and pattern recognition*, pages 586–595, 2018. [6](#)
- [61] Xin Zhang, Anpei Chen, Jincheng Xiong, Pinxuan Dai, Yujun Shen, and Weiwei Xu. Neural shell texture splatting: More details and fewer primitives. In *Proceedings of the IEEE/CVF International Conference on Computer Vision*, pages 25229–25238, 2025. [3](#)
- [62] Yangming Zhang, Wenqi Jia, Wei Niu, and Miao Yin. Gaussianspa: An “optimizing-sparsifying” simplification framework for compact and high-quality 3d gaussian splatting. In *Proceedings of the Computer Vision and Pattern Recognition Conference*, pages 26673–26682, 2025. [3](#)
- [63] Jianhao Zheng, Zihan Zhu, Valentin Bieri, Marc Pollefeys, Songyou Peng, and Iro Armeni. Wildgs-slam: Monocular gaussian splatting slam in dynamic environments. In *Proceedings of the Computer Vision and Pattern Recognition Conference*, pages 11461–11471, 2025. [1](#), [4](#)